SSRG International Journal of Electrical and Electronics Engineering
ISSN: 2348-8379/ https://doi.org/10.14445/23488379/IJEEE-V9I11P108

Volume 9 Issue 11, 67-94, November 2022

Original Article

Wind, PV Solar, Hydro and Hybrid Energy Storage System-Based Intelligent Adaptive Control for Standalone Distributed Generation System

Mulumudi Rajesh[1], A. Lakshmi Devi[2]

[1,2]*Department of Electrical and Electronics Engineering, Sri Venkateswara University College of Engineering, Tirupati, Andhra Pradesh, India.*

Corresponding Author: mrajeshjntuk@gmail.com

Received: 05 October 2022 Revised: 07 November 2022 Accepted: 20 November 2022 Published: 30 November 2022

Abstract *- With an isolated asynchronous generator (IAG), wind turbines or micro-hydro turbines power a self-contained distributed generating system. This system may be used independently or connected to the grid. Agritech is designed for use in remote areas without grid access. Fossil fuel depletion and environmental deterioration have impeded the power industry's development. Determining new energy sources and transforming energy production strategies is so critical. It will theoretically facilitate the world's largest single complementary demonstration project and test a massive multi-energy complementary system. These hybrid systems are made up of renewable energy and energy storage. Renewable energy is unknown. Thus supply sustainability and reliability are essential objectives. As a result, it reacts quicker than diesel generators and micro-turbines, reducing unpredictability. The battery may be utilized to keep things running when the power is turned out—Battery-super capacitor hybrid energy storage system with a centralized advanced neutral-fault-injection-switching (ANFIS) controller (SC). The battery's lifespan may be increased by increasing the amount of energy consumed over a longer period of time while simultaneously reducing the amount of stress placed on the battery. In this work, an individual implementation of P&O is used to calculate the MPOP for wind and solar PV arrays. Energy Storage System (ESS) adjusts the frequency of the stand-alone hybrid system using an adaptive neuro-fuzzy inference system (ANFIS) controller. All the necessary analysis, modelling, design work, and a simulated implementation in MATLAB for the suggested setup and control structure are included.*

Keywords *- Battery, Adaptive neuro-fuzzy inference system (ANFIS), Hydro, Hybrid Energy Storage (HES), Photovoltaic, Super capacitor and Wind.*

1. Introduction

Humankind has primarily utilized fossil fuels, including coal, oil, and natural gas recently. As power demand rises, fossil fuels are used at an alarming pace, polluting the environment. By 2030, energy demand should quadruple, and greenhouse gas emissions should reduce by 60% by 2050, according to the International Energy Agency. Developing renewable energy sources must be accelerated. Wind and solar power are clean, renewable energy sources. Solar and wind have continuously grown their percentage of overall energy since 2000. The proportion will be more significant than fifty percent by the end of the century [1]. Wind and PV power output is uneven, volatile, and difficult to govern. Increasing new energy power production is challenging and costly. Power may be generated locally using small hydro heads, wind, and solar energy. The voltage and frequency of small hydro-isolated asynchronous generators may be controlled using standard methods and an integrated adaptive neuro-fuzzy inference system (ANFIS) [2]. Because of their low cost, durability, brushless rotor design, and lack of dc supply, asynchronous generators have largely replaced synchronous ones. Because the asynchronous machine is separated, a VAR generator provides reactive power. Terminals commonly employ capacitor banks. A capacitor bank's rating is selected such that it generates rated voltage at rated speed with no load. Management of terminal voltage and frequency during load disturbances and power-quality difficulties are important limitations of small hydroelectric power generating systems compared to conventional generators. An uncontrolled small hydro turbine-driven generator needs an ANFIS with an appropriate control approach. Traditional hydropower is very controllable and has historically helped balance the power grid. In recent years, energy storage technology has improved quickly. Power fluctuations, peaks, and troughs in the distribution of fresh energy have been mitigated thanks to its adaptable adjustment mode and potent load-changing capabilities [3]. Multi-energy certainly complementing will increase energy efficiency and encourage energy transformation. The development boosts new energy consumption, improves energy efficiency, and supports

modern energy systems. The coexistence of numerous energy power- generating types is a trend, and a coordinated optimization method is needed. Rising new energy power demands need a coordinated multi-energy optimization technique. Academics have done a little study on hydropower, PV, wind, and battery storage. Most systems are wind-hydropower, PV-hydropower, wind-PV-hydropower, or wind-PV-storage. These systems are for remote areas alone. Reference analyses the new energy consumption based on the current status of use. It also emphasizes wind and solar abandonment factors. Find an alternative system that also produces new energy. A daytime scheduling model for hydropower and PV is provided in reference, with the most incredible output during peak demand. Wind energy's resource advantages were not considered. Rain lowers PV output. Wind energy will be needed if the reservoir is not fixed quickly. In reference, the best scheduling technique for complimentary hydro water, wind, and PV systems was explored to avoid damaging the reservoir and abandoning water. Hydropower should be utilized for flood control, irrigation, and lowering wind power's unpredictability. Hydrogen-based thermal energy storage (HRES) in these micro power plants, which are mainly based on renewable sources and energy storage systems (ESS), has various benefits over bigger power plants, including environmental friendliness, superior power quality, and scalability [4]. A traditional HRES system includes hydroelectric power, wind turbines, solar panels, and other renewable energy sources. Hydroelectricity, wind, or solar radiation are used to create electricity when accessible. Since solar irradiance, wind speed, and hydroelectric power generation are unpredictable, a backup energy source is needed to improve the HRES' controllability and operability. A battery and supercapacitor system is employed. They help maintain the equilibrium between supply and demand by compensating for primary energy surpluses and renewable energy deficits [5].

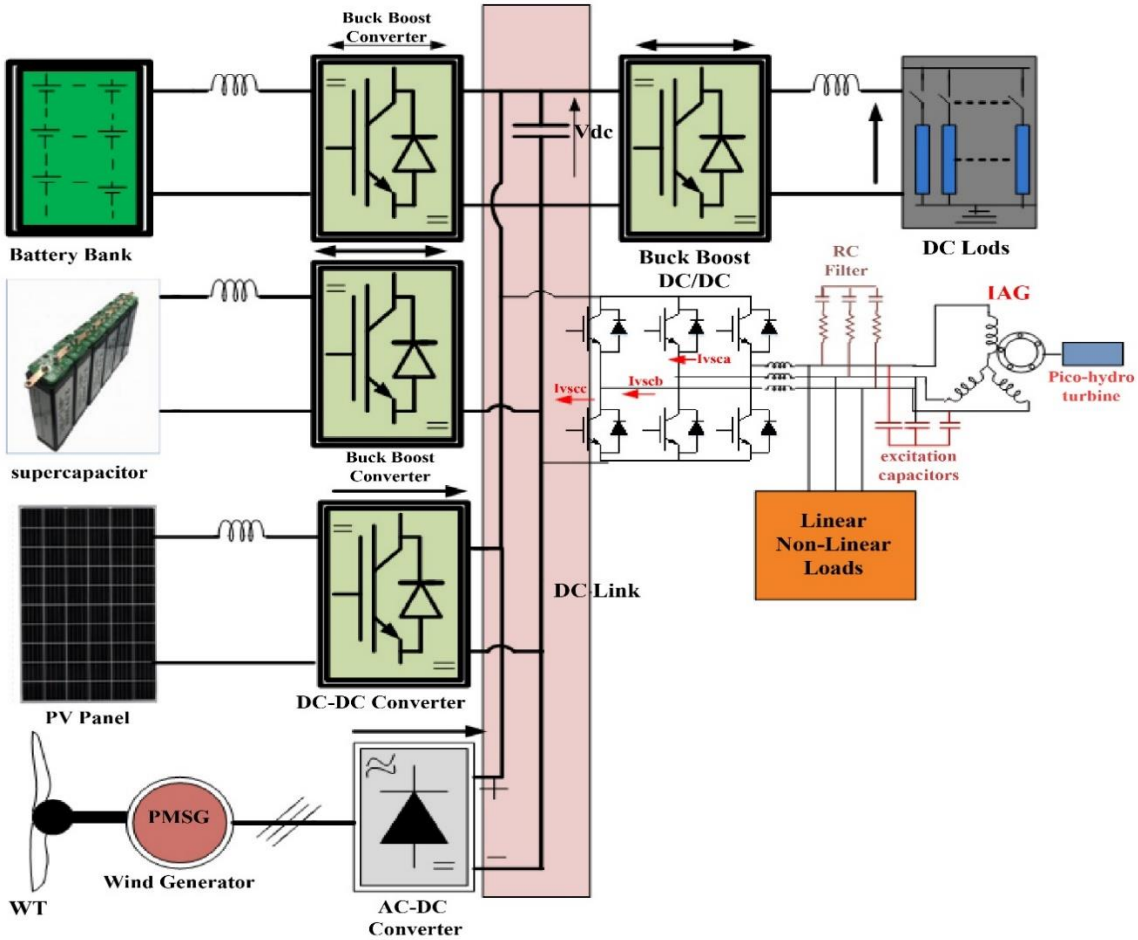

Fig. 1 Proposed configuration of the hybrid energy storage system

A traditional ESS, such as a battery and supercapacitor system, is used to do this. They are considered an effective method of balancing production and demand, allowing for supporting renewable energy shortages when necessary and storing primary energy overflows when possible, among other things. HRES has a two-tiered control architecture that it shows. In this case, the supervisory control system ensures that the ESS has the power it needs to do its job at the highest

level [27]. Direct control of the converters that link renewable energy sources to the ESS ensures that the energy sources function as this control system requires. Due to advancements in renewable energy technology and power systems, most research on HRES control structures addresses independent operation at isolated sites [7]. Electronic converters translate renewable energy's unregulated power into a form usable at the load. Both conventional and intelligent control methodologies were employed to assess the HRES's control system. Conventional control techniques (such as PID or state machine controllers) demand a thorough mathematical description of the system. The effectiveness and resilience of neuro-fuzzy systems, convolutional neural networks, and fuzzy logic systems are significantly higher. Classical approaches improve the system's dynamic behavior without requiring a flawless model. This research used ANFIS because it converges faster than other neuro-fuzzy models. Grid-connected HRESs are less well-documented than stand-alone HRESs.

No references to ANFIS in the supervisory control system have been found. ANFIS controls hydroelectric inverters. Compares the PI controller and ANFIS controller for single-phase inverter regulation. Three-phase inverter ANFIS controller feasibility was investigated in [8], where dc bus voltage and reactive power were employed to manage the load. It features a three-phase inverter controlled by an ANFIS and an energy management system (EMS) for a hybrid renewable energy system (HRES) that includes a supercapacitor and a battery [9]. Key contributions include: ANFIS estimates the power necessary to be produced and stored in the ESS (supercapacitor and battery) based on the loads' energy needs, available power sources, and SOCs of supercapacitors and batteries. It also controls the three-phase inverter's power delivery.

2. Design and Configuration of Hydro/Wind/ Photovoltaic/Energy Storage System

Separate dc-dc and ac-dc converters join PV, wind, and hydropower generators to produce a hybrid power system. The DC-DC converter is fueled by solar panels and receives input from the diode bridge rectifier. A hybrid system is formed when DC link bus capacitors are combined with other energy sources. Fig. 1 shows that the proposed hybrid energy system includes an independent hydropower generator. The VSI transfers extracted power to AC loads while the battery bank and supercapacitor store excess power. Inductors connect VSI to the hydro generator and PCC loads (L_f). An IAG capacitor bank provides reactive power for voltage building. This MPPT control system uses tracing algorithms to maximize PV and wind power simultaneously. The following subsections address PV system modelling, wind system modelling, and Boost converter construction

3. Mathematical Description of the Hybrid Energy System

3.1. Isolated Hydro Generation System

3.1.1. Hydroelectric Output Model

A hydropower plant is a manufactured structure that uses water to generate electricity. The water head is created by channeling the water flow into the building, directing it to the turbine, and turning the turbine and generator together to harness the potential energy of the water flow and convert it into electricity [10]. Effectively converting the potential energy lost as water flows downstream into usable electricity is known as:

$$P_{H,t} = \frac{\rho_H g V \eta h}{t} = 1.8 Q \eta h \qquad (3.1)$$

P_{Ht} is the amount of electricity generated by hydroelectric dams during the time period t; h represents the difference in water level between the upstream and downstream locations; ρ_H denotes the density of the water, while Q refers to the flow velocity of the water. There is a correlation between the amount of precipitation in the atmosphere, runoff in rivers, storage space in reservoirs, and the features of turbines. Since the precipitation in the atmosphere and the flow of the water are not expected to fluctuate significantly for a short amount of time (such as one day or a few hours), the short-term dispatching of the hydropower plant will remain steady.

3.1.2. Design of the IAG

The majority of single-phase loads are rated at 230 or 220 volts, respectively. For the purpose of feeding these single-phase loads, an IAG with three phases and four poles at 415 volts and 50 hertz has been devised and constructed. The selection of excitation capacitors for a single-phase power production system using a three-phase IAG is the first step in the excitation capacitors, as follows.

3.1.3. Selection of Excitation Capacitors

[11, 12]Describe the excitation capacitors needed for a three-phase IAG to operate in balance and provide the rated terminal voltage. An IAG's rated terminal voltage may be maintained by the amount of capacitive reactance Xc needed per phase. It is necessary to calculate the three-phase capacitive reactive power in the following way in order to attain the rated IAG voltage at the rated resistive load and speed:

$$Q = 3V^2 / x_c \qquad (3.2)$$

Excitation capacitor bank 4.3 kVAR delta-connected for 3.7 kW four-pole 50Hz IAG is employed.

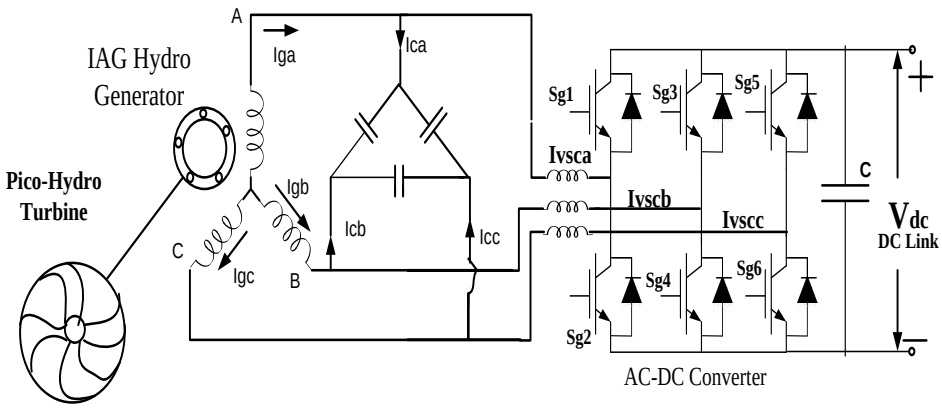

Fig. 2 Schematic diagram of the hydro generation system

Fig. 2 demonstrates how the hydro converter works with wind, PV, batteries, and supercapacitors. Adaptive neuro-fuzzy inference systems are being developed (ANFIS). It controls the battery, supercapacitor, DC-link voltage, wind/PV terminal voltage, and PCC output power (point of common coupling). "Vbat_ref" refers to a battery, supercapacitor, Vdc DC-link voltage, PCC voltage, and output power. Fig.3 shows the direct (d) and quadrature (q) PCC voltages, Vd and Vq. ILd and ILq are the direct and quadrature load currents. Id and Iq are the direct and quadrature inverter currents. Adaptive neuro-fuzzy inference system (ANFIS) controllers manage PCC voltage and power. Vabc and Iabc are the three-phase (PCC) voltage and inverter current, respectively.

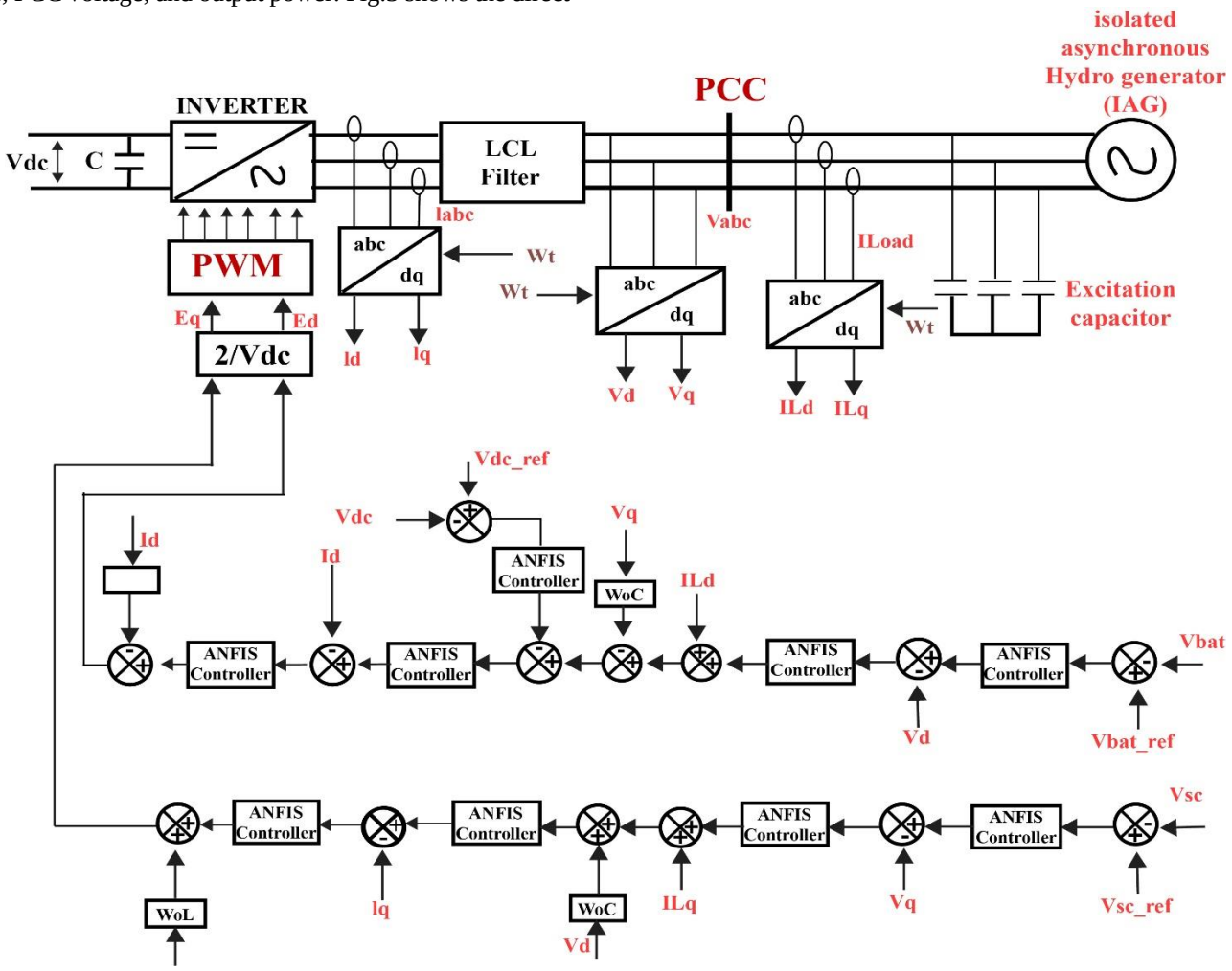

Fig. 3 Control strategy for VSC

4. Solar Power System Model

With the use of a PV model, we will demonstrate how to construct a hybrid renewable energy system in the next section. This article looks at a single-diode equivalent model of a PV cell, similar to the one illustrated in Fig. 4, as can be seen in Fig. 4. To represent a PV system mathematically, the fundamental I PV-V PV properties of a PV panel are utilized.

4.1. Single Diode Solar PV Equivalent Circuit Models

Equivalent circuit models show the I-V curve of a cell, module, or array for a certain operating condition. As an example, look at a circuit for a single solar cell:

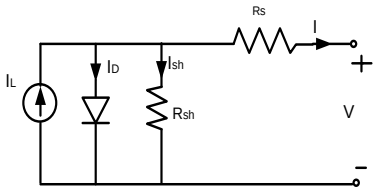

Fig. 4 Equavalent model of PV solar

Kirchhoff's current law for current has been incorporated into the derivation of the equation that governs this analogous circuit.

$$I = I_L - I_D - I_{sh} \tag{4.1}$$

Light-generated current is referred to as IL; ID refers to the voltage-dependent current lost due to recombination, whereas Ish refers to the current loss due to shunt resistances. In this model of a single diode, the value of ID is represented by the Shockley equation, which describes an ideal diode:

$$I_D = I_0 \left[\exp\left(\frac{V+IR_s}{nV_T}\right) - 1\right] \tag{4.2}$$

In this equation, n represents the diode's ideality factor (usually between (4.1) and (4.2) for a single junction cell), I 0 represents the saturation current, and V T represents the thermal voltage.

$$V_T = \frac{kTc}{q} \tag{4.3}$$

Where k is Boltzmann's constant $1.381 \times 10^{-23} J$ / k and q is the elementary charge 1.602×10^{-19} C. Writing the shunt current as $I_{sh} = (V + IR_s) / R_{sh}$ and the whole governing equation for the single diode model is obtained by combining this with the previous two equations.

$$I = I_L - I_0 \left[\exp\left(\frac{V+IR_s}{nV_T}\right) - 1\right] - \frac{V-IR_s}{R_{sh}} \tag{4.4}$$

Models of single-diode equivalent circuits rely on these five parameters, expressed in this equation. I_L: Intensity of Light (A) Saturation current in the opposite direction of a diode, denoted as I_0 (A) Series resistance: R_s (Ω) Resistance of the shunt: R_{sh} (Ω) Assuming that all cells in a photovoltaic module or array have the same characteristics and are exposed to the same amount of irradiance and temperature, we may calculate how much power each cell produces (i.e., generate equal current and voltage) I_module=I_cell, and V_module=N_s×V_cell.

The module or array's single-diode equation is as follows:

$$I_M = I_L - I_0 \left[\exp\left(\frac{V_M+I_M\ N_sR_s}{nN_sV_T}\right) - 1\right] - \frac{V_M+I_MN_sR_s}{N_sR_{sh}} \tag{4.5}$$

Where I_M and V_M indicates the module's or array's voltage and current. Careful implementation of model parameters is required since they may affect a single cell, a module, or a whole array. Since the single diode equation for I is the most often used variant, it is the only one that may be used with the module and array parameters.
The thermal voltage V T, the diode ideality factor n, and the number of series cells N s may all be merged into a single variable 'a,' which is known as the modified ideality factor:

$$a = \frac{N_snkTc}{q} \tag{4.6}$$

The process for making comparable circuit modules was given. As cell temperature and irradiance vary, auxiliary equations show how single-diode equation parameters change. Auxiliary equations are these equations. Instead of cells or arrays, we'll concentrate on PV modules to comprehend PV modelling software. PV modelling software uses module models to predict solar panel performance [9].

4.2. P&O-Based MPPT Algorithm for Solar PV System

[13] As shown in Maximum power point tracking (MPPT) using a Perturb and Observe approach is shown in Fig. 6. This MPPT approach optimizes a PV array's voltage to generate the greatest power. PV array voltage and energy storage voltage are used to compute the boost converter switch's reference duty ratio. Fig. 5 shows how to construct a boost converter gate pulse. This estimate helps the researcher get through the Perturb stage, during which the perturbation moves the search point along the solar characteristic curve. ANFIS controller creates V PWM (Sref). An ANFIS controller gives the adaptive control system operation and adaptation flexibility. ANFIS controller inputs power production problems.

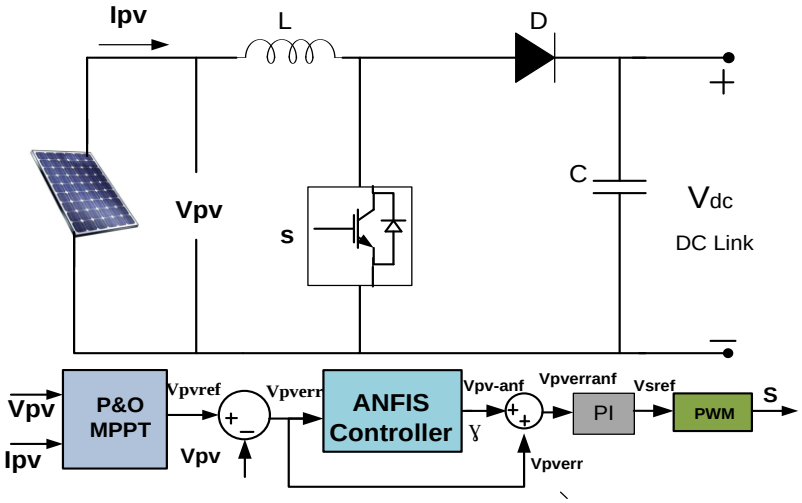

Fig. 5 Solar energy system with controller

$$V_{PVerr}(n) = V_{PVref}(n) - V_{PV}(n) \quad (4.7)$$

Based on the ANFIS tuning output $\gamma(n)$ is given as

$$\gamma(n) = \Gamma[V_{PV}\text{anf}\,(n), \Delta V_{PV}\text{anf}\,(n)] \quad (4.8)$$

Where γ (n) is the new voltage improvement parameter for MPPT as specified by ANFIS, the voltage used for establishing standards is listed here:

$$V_{PVerr}\text{anf}\,(n) = V_{PVerr}(n) + \gamma(n) \quad (4.9)$$

The PI controller output provides V_{sref} as,

$$V_{sref}(n) = V_{sref}(n-1) + k_i[V_{PVerr}anf(n) - V_{PVerr}anf(n-1)] + k_P[V_{PVerr}anf(n)] \quad (4.10)$$

ki and kp, respectively, are the PI controller gains. With the use of the ANFIS controller, solar electricity can be better regulated and tracked more quickly. (V_{sref}) is shown in Fig. 5 as the power-generating ingredient. For the PV solar MPPT dc to dc converter controller, gating pulses (S) are created by the switching signal generator.

5. Wind System Model

5.1. Wind Turbine Modeling

With its aerodynamic design, the blades convert the wind's kinetic energy into mechanical energy that powers the generator. So, we can calculate the aerodynamic torque T a using [14]:

$$T_a = \frac{1}{2\omega_r}\rho A V_w^3 C_P(\lambda, \beta) \quad (5.1)$$

The figure shows the air pressure, wind speed, and surface area. The power coefficient of a wind turbine varies from one to another because of its pitch angle and tip speed ratio. This is how each turbine creates energy for the grid. The power coefficient can be represented as

$$C_P(\lambda, B) = C_1\left(\frac{C_2}{\lambda_i} - C_3 B - C_4\right)e^{\frac{-C_5}{\lambda_i}} + C_6\lambda \quad (5.2)$$

$$\frac{1}{\lambda_i} = \frac{1}{\lambda + 0.08\beta} - \frac{0.035}{\beta^3 + 1} \quad (5.3)$$

Where $\lambda = \frac{\omega_r R}{Vw}$ and C1=0.5176; C2=116; C3=0.4; C4=5; C5=21; C6=0.0068;

Low shaft speed in a wind turbine's dynamic drivetrain system is caused by torsion and friction. To keep things simple, we represent the wind turbine's drivetrain as a single mass by assuming the low shaft speed is relatively stiff.

The first-order equation that describes this dynamic may be written as:

$$\dot{\omega}_r = \frac{T_a}{J_t} - \frac{T_{em}}{J_t} \quad (5.4)$$

Where J_t is the inertia, $\dot{\omega}_r$ is the rotor speed and T_{em} is the electromagnet generator torque.

5.2. Permanent Magnet Synchronous Generator Modeling

This model is designed in accordance with the Park d-q rotation frame and coupled to the rotor [28].

$$\begin{cases} v_d = R_s i_d + L_d\frac{di_d}{dt} - L_q i_q \omega_e \\ v_q = R_s i_q + L_q\frac{di_q}{dt} + L_d i_d \omega_e + \omega_e \phi \end{cases} \quad (5.5)$$

Where v_d and v_q are the voltages, i_d and i_q are the currents along the d and q axis, respectively, R_s is the stator resistance $L_d = L_q$ are the inductance of the generator, ϕ is

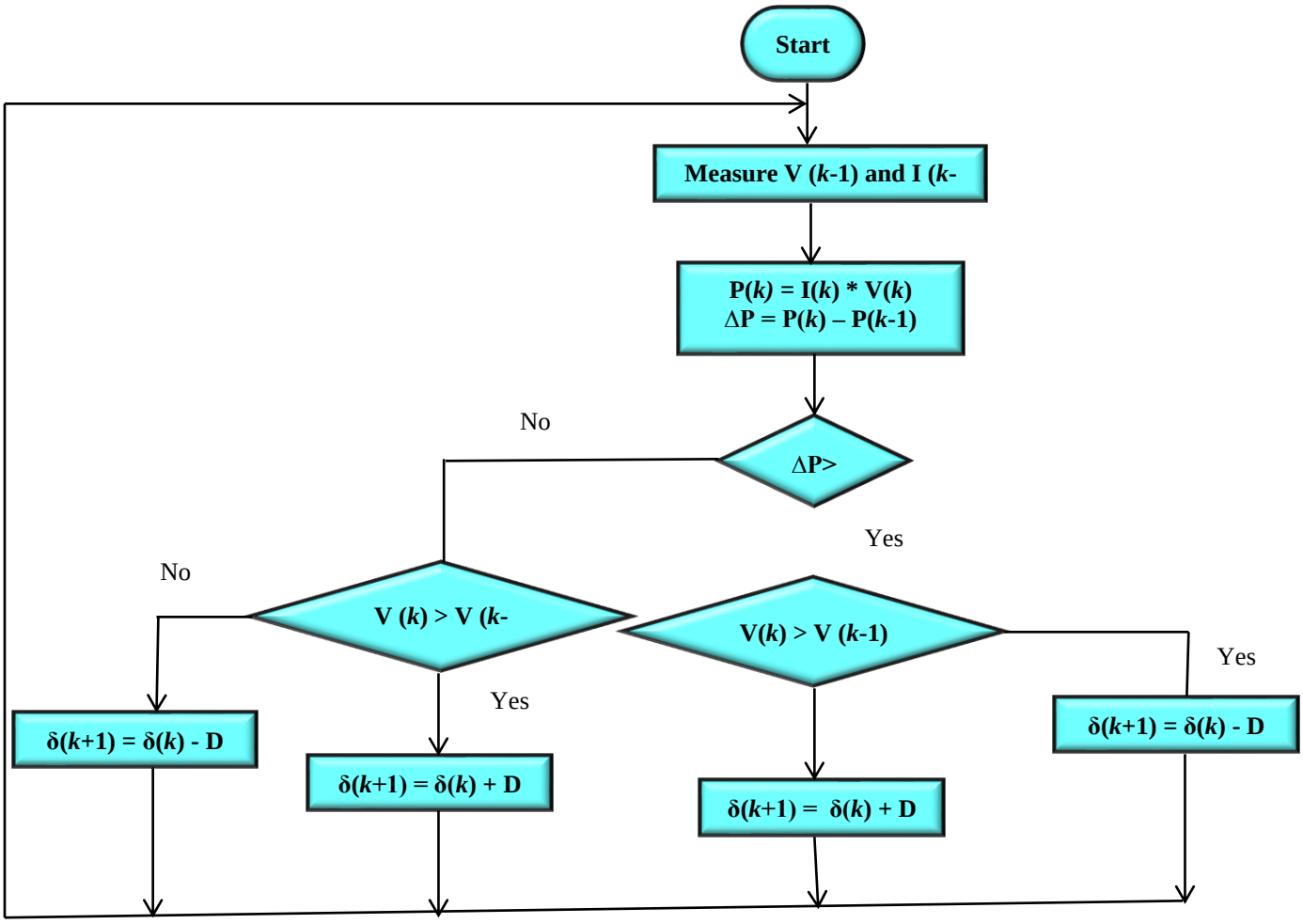

Fig. 6 Flowchart of the P&O method for MPPT

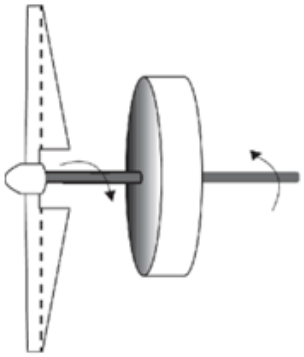

Fig. 7 Depicts a single-mass drivetrain

the permanent magnet flux, $\omega_m = \frac{\omega_e}{P}$ is the electrical rotating speed of the generator in which P is the number of pole pairs. The electromagnet torque equation can be written as follows:

$$T_{em} = \frac{3}{2}P\left[\left(L_d - L_q\right)i_d i_q + i_q\phi\right] \quad (5.6)$$

When the PMSG is driven by direct current, the difference between inductances D and Q tends to be zero [16]. Then, the electromagnet's torque is only affected by the current on the q-axis and not the other way around. Eq. (5.1) can be changed into Eq. (5.2):

$$T_{em} = \frac{3}{2}Pi_q\phi \quad (5.7)$$

5.3. MPPT Algorithm for WECS

Fig. 9 shows a typical wind turbine system with a turbine, PMSG generator, a generator-side converter that converts AC to DC, and a boost converter that enhances output voltage. It also incorporates a VSC converter-side converter to boost output power. Inverter output may be used to power distribution system loads. The perturbation drives the search point on the wind characteristic curve, while the estimate accounts for wind velocity variation. The ANFIS controller produces PWM [17]. The ANFIS controller is utilized for adaptive control since it is flexible. ANFIS controls the produced electricity.

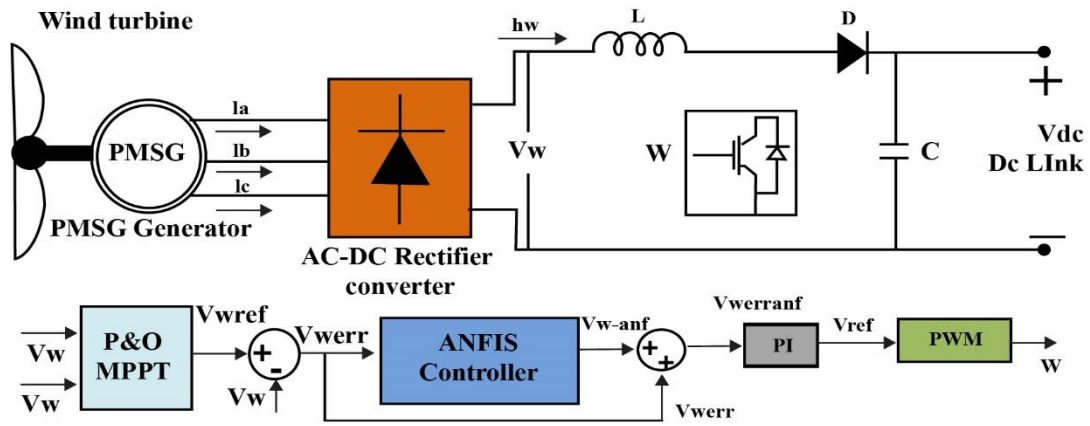

Fig. 8 Wind energy system with controller

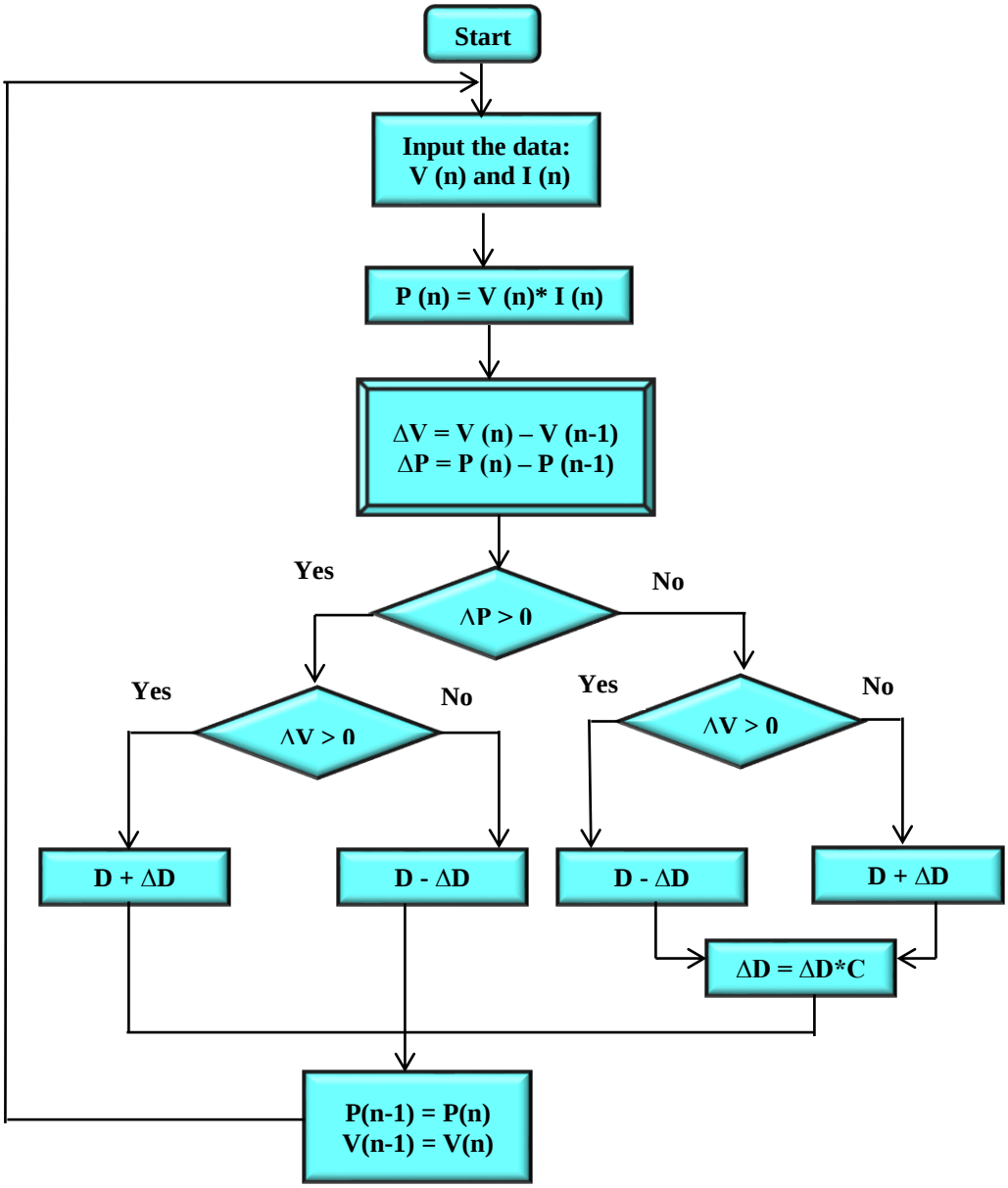

Fig. 9 Flow chart of perturb and observe algorithm

$$V_{werr}(n) = V_{wref}(n) - V_w(n) \quad (5.8)$$

Based on the ANFIS tuning output $\gamma(n)$ is given as

$$\gamma(n) = \Gamma[V_w\text{anf}\,(n), \Delta V_w\text{anf}\,(n)] \quad (5.9)$$

Where $\gamma(n)$ the new and enhanced MPPT voltage parameter is made available by ANFIS. The reference generation voltage is provided as

$$V_{werr}\text{anf}\,(n) = V_{werr}(n) + \gamma(n) \quad (5.10)$$

The PI controller output provides w_{ref} as,

$$V_{sref}(n) = V_{sref}(n-1) + k_i[V_{PVerr}anf(n) - V_{PVerr}anf(n-1)] + k_P[V_{PVerr}anf(n)] \quad (5.11)$$

Gains are expressed as ki and kp. The ANFIS controller helps regulate and monitor wind power. Fig. 8 shows how W ref is created. Wind power is transmitted to the switching signal generator to acquire the controller's gating pulses (W).

6. Battery System Model

6.1. ESS Batteries

The energy storage system utilizes Li-ion batteries. Li-ion batteries are the industry standard. There is a dearth of information on ESS for CS, so the decision was based on two points supported by [18]: (1) Li-ion batteries have a very high efficiency (85-95 percent), high energy density, and high number of life cycles (3,000-5,000); and (2) Li-ion batteries as ESS have already been used in a real implementation of an ESS fast CS, which showed good

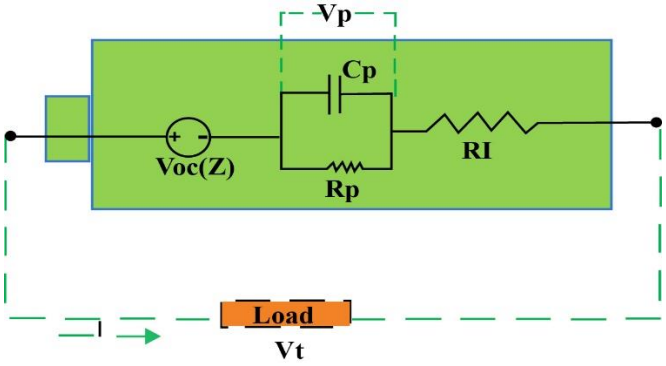

Fig. 10 Li-ion Battery Equivalent Circuit Model

We can simulate ESS batteries with Simulink (see Fig. 2b). Change battery specifications to match commercial datasheets. This type features a changeable voltage source and resistance. Open circuit battery voltage, Ebat, differs from internal battery resistance, Rint. It is the difference between Ebat and Rint. Ebat and Rint vary by battery type [19].
State of Charge Equation:

$$z(t) = z(0) - \frac{\int_0^t I(\tau)\,d\tau}{Q_{max}} \quad (6.1)$$

$$z(t) = -\frac{I(t)}{Q_{max}} \quad (6.2)$$

Model Equation:

$$V_P(t) = -\frac{V_P(t)}{R_P C_P} + \frac{I(t)}{C_P} \quad (6.3)$$

$$V_t(t) = V_{oc}(z) - V_P - I(t) \cdot R_I \quad (6.4)$$

6.2. Li-ion Battery Circuit Model

In addition to the charge state, Z(t), open-circuit voltage, Voc(z), and polarisation voltage, Vp(t), RI can also be expressed as Calculating Total Internal Resistance (R), Load Current (A), and Terminal Voltage (Vt). The Li-ion Battery Equivalent Circuit Model depicts the reduction in useable voltage caused by polarisation and the cell's internal IR drop. Open-circuit voltage is only reached, and the maximum amount of theoretically accessible energy is delivered while operating at extremely low currents when polarization and IR loss are minimal.

$$V_t(t) = V_{oc}(z) - V_P - I(t) \cdot R_I \quad (6.5)$$

The maximum battery capacity, Q, is used to indicate the SOC of the battery in the basic coulomb-counting method (Eq. (6.6)).

$$SOC(\%) = SOC_0(\%) - 100\left(\frac{\int \mathrm{I_{bat}}\cdot \mathrm{dt}}{\mathrm{Q}}\right) \quad (6.6)$$

This model's charging and discharging dynamics are quite close to the experimental behavior, with only minor inaccuracies for states of charge (SOC) between 100% and 20%. Using this study's control, the battery can work between 20% (to avoid deep discharge) and 100% SOC. SOC is commonly determined using Coulomb counting. Li-ion batteries (used in this experiment) have fewer adverse effects than other varieties. The present integration of this approach is severely flawed due to a cumulative inaccuracy. In this strategy, the sensor's current accuracy determines its accuracy. Cumulative current measurement errors may generate inaccuracies over time. Inaccuracies in the current measurement and SOC are ignored [20].

6.3. BESS Converter Configuration

A hybrid system must establish a proper voltage level to avoid unnecessary conversion steps and provide constant, efficient energy delivery. Hydropower, wind, and solar panels provide the hybrid system's electricity. As indicated in Fig. 11, the ESSs are linked to the DC bus through a bidirectional Dc-Dc converter (BDC). Dc-Dc converters eliminate DC voltage fluctuations when utilized between a DC bus and a battery. The system's efficiency, reliability, and dynamic performance depend on the bidirectional converter functioning in various modes, allowing its many components to operate as efficiently and reliably as feasible.

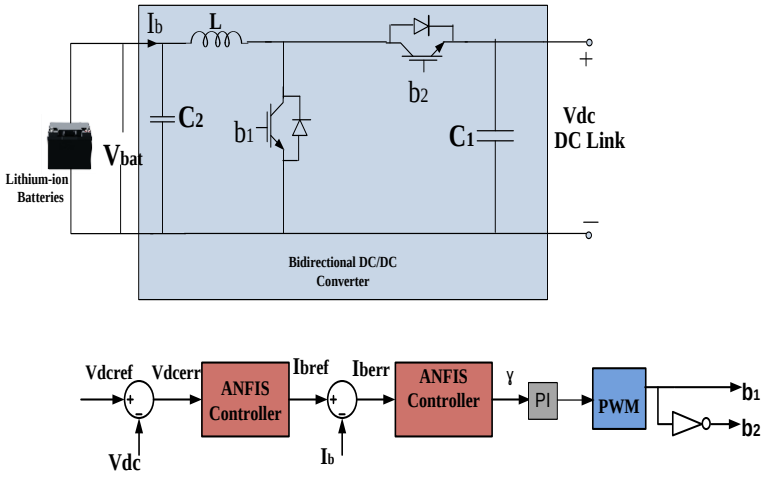

Fig. 11 A battery storage system with a controller.

7. Supercapacitor Modeling

Supercapacitors have ion-permeable separators between their electrodes. The advantages of these batteries include high density, energy efficiency, low internal resistance, long cycle life, and fast charging and discharging times. As supercapacitors become more popular, several circuit models have arisen—an energy-storing capacitors. The discharge-charge cycle may be continued practically indefinitely as long as the charge is retained. Electrochemical capacitors (ECs), also called supercapacitors, ultra-capacitors, and electric double-layer capacitors, have the highest capacitance values (EDLC). 400 Farads may charge normal-sized cases concurrently. Supercapacitors offer the greatest capacitive density possible, enabling them to replace batteries. Supercapacitors are preferred over batteries when storing and using enormous amounts of energy in bursts.

7.1. Conceptualization of a Super Capacitor-Based Energy Storage System

The overall capacitance of the storage system should be considered when estimating the number of series supercapacitors and parallel capacitors for the Super capacitor energy storage system [29]. Voltages in supercapacitors may be determined using this formula: V Cell = V Capacitor Voltage

$$V_{scmax} = n_s * V_{Cell} \tag{7.1}$$

Where n_s is the number of supercapacitor cells in a series; together, they form a string. In the same manner R_{Cell} is the equivalent series resistance, then the series ESR of the string is given by

$$R_s = n_{s^*} R_{Cell} \tag{7.2}$$

Series capacitance (Cs) of n_s individual series supercapacitor cell in the string is given by

$$C_s = \frac{C_{Cell}}{n_s} \tag{7.3}$$

The nominal current in the supercapacitor bank is I_{scmax} is given by the formula

$$I_{scmax} = \frac{I_{scmax}}{I_{Cell}} \tag{7.4}$$

Where P_{sc} the supercapacitor bank is rated power Current in each series string (I_{Cell}) of n_s series supercapacitor cell is less than I_{scmax}. with help of I_{scmax} and I_{Cell} number of series strings in parallel can be given by

$$n_p = \frac{I_{scmax}}{I_{Cell}} \tag{7.5}$$

Equivalent super capacitance due to n_p resistance of each C_s

$$C_{sc} = n_{p^*} C_s \tag{7.6}$$

Equivalent series resistance (R_{sc}) due to n_p of each R_s

$$R_{sc} = \frac{R_s}{n_p} \tag{7.7}$$

The energy of the supercapacitor (E_{sc}) with the help of V_{sc} and C_{sc}

$$E_{sc} = \frac{1}{2} * C_{sC} * V_{sc}^2 \tag{7.8}$$

Supercapacitor capacitance (C_{sc}) can be calculated using the nominal voltage (maximum voltage) V_{scnom} and minimum voltage V_{scmin} by

$$C_{sc} = \frac{2 * P_{sc^*} t_d}{(V_{scnom} - V_{scmin})^2} \tag{7.9}$$

Where $E_{sc} = P_{sc^*} t_d$

7.2. RC Circuit Model

The RC model of an ultra-capacitor is shown schematically in Fig. 12. This circuit comprises the following three components: Csc is the capacitance of the ultra-capacitor, Rp is the parallel resistance, and Rs is the corresponding series resistor for charging and discharging. This model has been tested and shown to be accurate in several studies. According to this definition, the dynamic is

$$\frac{du_1(t)}{dt} = \frac{-u_1(t)}{R_P C_{SC}} + \frac{I_{SC}}{c_{SC}} \tag{7.10}$$

$$V_{sc}(t) = R_s I_{SC} + u_1(t) \tag{7.11}$$

7.3 Converting between direct Current and Alternating Current using a Supercapacitor

A converter is needed to connect the DC and AC lines, as the supercapacitor cannot directly power the grid. The inductor and supercapacitor are linked in series to smooth the current. The SCESS circuit is shown in Fig. 13. It needs two IGBT switches. IGBTs connected in shunt mode give a boost mode switch, while IGBTs connected in series mode provide a buck mode switch. The circuit has four modes of operation. Boost mode utilizes DC link voltage to charge the supercapacitor, whereas buck mode uses it to discharge it [30].

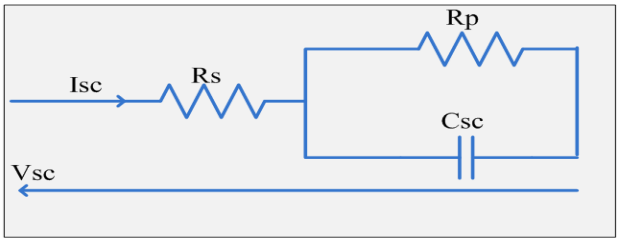

Fig. 12 Supercapacitor Equivalent Model.

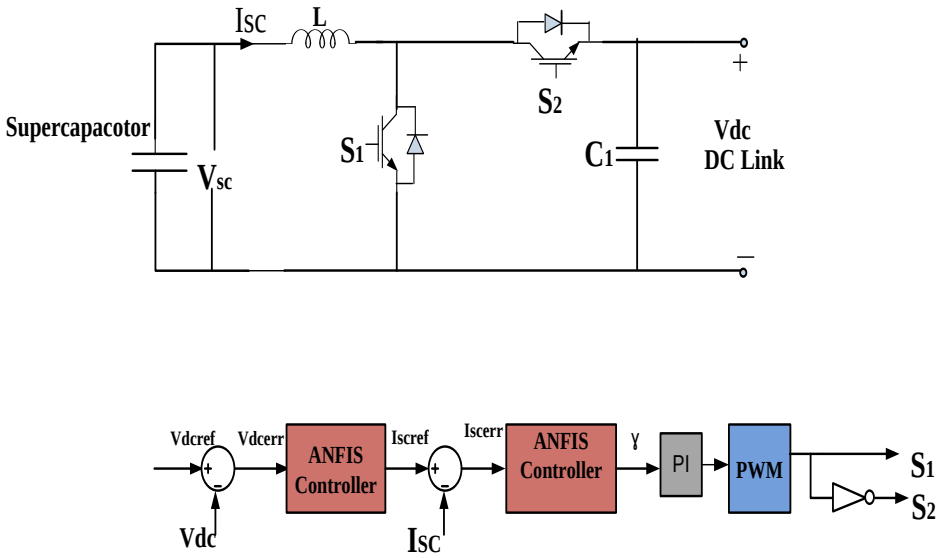

Fig. 13 Supercapacitor energy storage system with controller.

8. Proposed Controller Design Process

Two control loops provide VSC and power-sharing between HESS and DC (voltage and current). ANFIS and PI Controllers are intended to achieve results.

8.1. ANFIS Controller

ANFIS controller was created using system identification methods. Fig. 3 shows the suggested control architecture. Fig. 14 shows the ANFIS controller's design. Five-layer design has an input, a hidden, and two output layers [23]-[25].
Takagi-Sugeno ANFIS's guidelines declare,

$$IF \Delta e = x_1 \& \frac{d}{dt}\Delta e = y_1, THEN f_1 = a_1 \Delta e + b_1 \frac{d}{dt}\Delta e + k_1 \tag{8.1}$$

$$IF \Delta e = x_2 \& \frac{d}{dt}\Delta e = y_2, THEN f_2 = a_2 \Delta e + b_2 \frac{d}{dt}\Delta e + k_2 \tag{8.2}$$

The parameters a1, a2, b1, and b2 are held constant, but the sets x1, x2, and y1, y2 are fuzzy. In the following, each layer is described in detail.

The first layer receives the majority of the input variables and generates the corresponding fuzzy sets of output variables and functions based on the following:

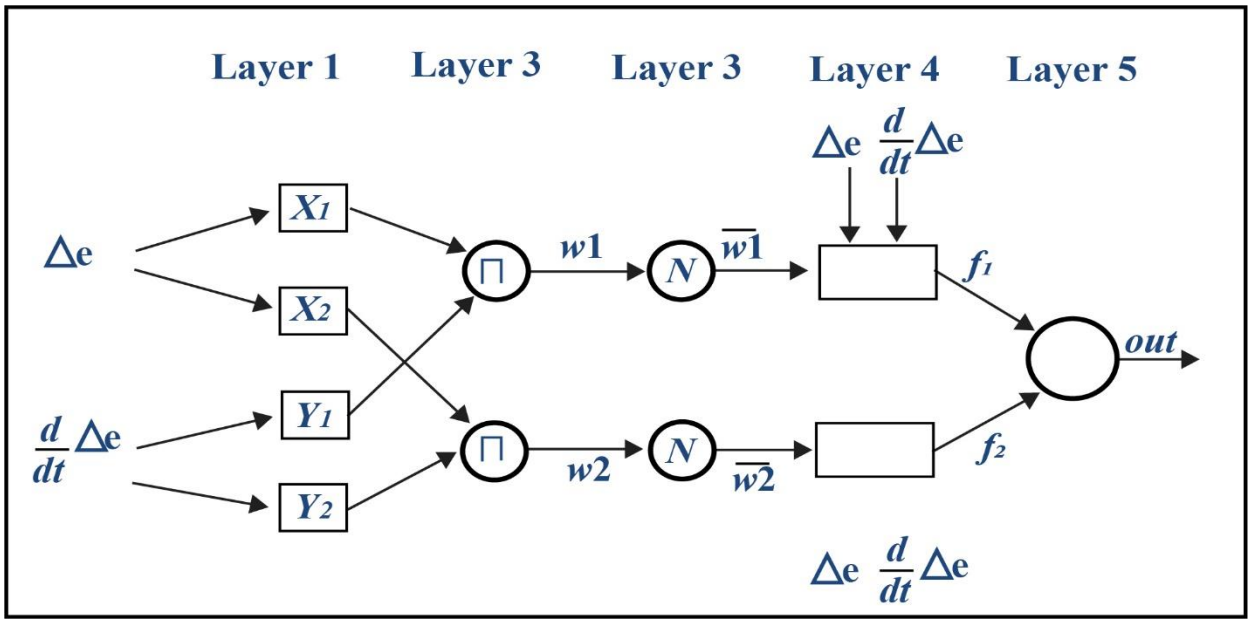

Fig. 14 ANFIS architecture

$$Out_i = \mu x_i(\Delta e) \tag{8.3}$$

$$Out_i = \mu y_i\left(\frac{d}{dt}\Delta e\right) \tag{8.4}$$

The Gaussian output membership is denoted by outi, where xi and yi are the node's linguistic levels.

Function (MF) of the linguistic levels of the ith node. The Gaussian Multiplier Function (MF) is defined as:

$$\mu x_i(\Delta e) = e^{-0.5\left(\frac{x-c}{\sigma}\right)^2} \tag{8.5}$$

$$\mu y_i\left(\frac{d}{dt}\Delta e\right) = e^{-0.5\left(\frac{x-c}{\sigma}\right)^2} \tag{8.6}$$

Where σ and c, respectively, denote the width and the center of the membership function.

Multiplying the output signals from layer 1 by the input signals from layer 1 constitutes layer 2. The layer 2 output may be modelled as follows:

$$Out_{2,i} = W_i = \mu x_i(\Delta e) \times \mu y_i\left(\frac{d}{dt}\Delta e\right) \tag{8.7}$$

Where, W_i represents the firing node of each node.

Most of the nodes in Layer 3 are shaped like circles. In this case, there is no difference between the total number of fuzzy rules and the number of layers. The output of the ith node is governed by one of 25 fuzzy rules based on the ith node's weighted firing strength relative to the sum of all firing strengths. Layer 3 output looks like this:

$$Out_{3,i} = W_i^{'} = \frac{w_i}{\sum(w_1 - w_2)} \tag{8.8}$$

At the fourth and final layer, we may derive the functions of the nodes that produced the outputs by:

$$Out_{4,i} = f_1 = W_1'\left(a_1\Delta e + b_1\frac{d}{dt}\Delta e + k_1\right) \tag{8.9}$$

$$Out_{4,i} = f_2 = W_2'\left(a_2\Delta e + b_2\frac{d}{dt}\Delta e + k_2\right) \tag{8.10}$$

On the fifth and final layer, the ANFIS's final output is computed by adding the signals from the four previous layers, as shown here:

$$Out_{5,i} = Out = \sum(f_1 + f_2) \tag{8.11}$$

9. Results and Discussion

A DGS is created in the simulation in MATLAB/Simulink to illustrate the efficacy and resilience of the novel control system.

9.1. Constant-load Steady-State Performance of a Hypothetical Hybrid System

The hybrid system operates at total capacity to fulfil the load requirements. The amount of wind-generated is proportional to the wind's velocity. As shown in Fig. 15, the amount of energy created decreases as wind speeds decrease. Figure 15 depicts the results of this analysis. The PMSG currents and generation both increase with increasing wind speed. It can be seen clearly in Fig. 15. During this time, PMSG runs regularly. It takes a lot of time. At t = 2s and t = 2.5s, the wind speed goes from 7.2 m/s to 12 m/s.

9.2. The Effect of Wind Speed Variability on Behavior

To meet demand, the isolated hybrid system employs renewable energy. A significant drawback of renewable energy production is the unpredictable nature of its output. In addition, the local load demand fluctuates throughout the day. The isolated hybrid system's control algorithms are flexible enough to fulfil all the requirements and supply the required load. Fig. 16 and 16 (a) Wind speed at t = 1.9s and t = 2.2s illustrates the PMSG current and power change with wind velocity. Wind turbines create more electricity when the wind speed increases, and currents and power increase as a result. As wind speed decreases, so does wind production, and the battery and supercapacitor, which were originally charging, are now discharging themselves. Fig. 16 depicts the battery and supercapacitor dynamic behavior (b). When wind speeds are low, the SG's output of electricity drops and the battery and supercapacitor make up the resulting shortfall. Fig. 16 depicts how the hybrid system's power stays constant despite changes in the PV power, dc-link voltage, and IAG power (c).

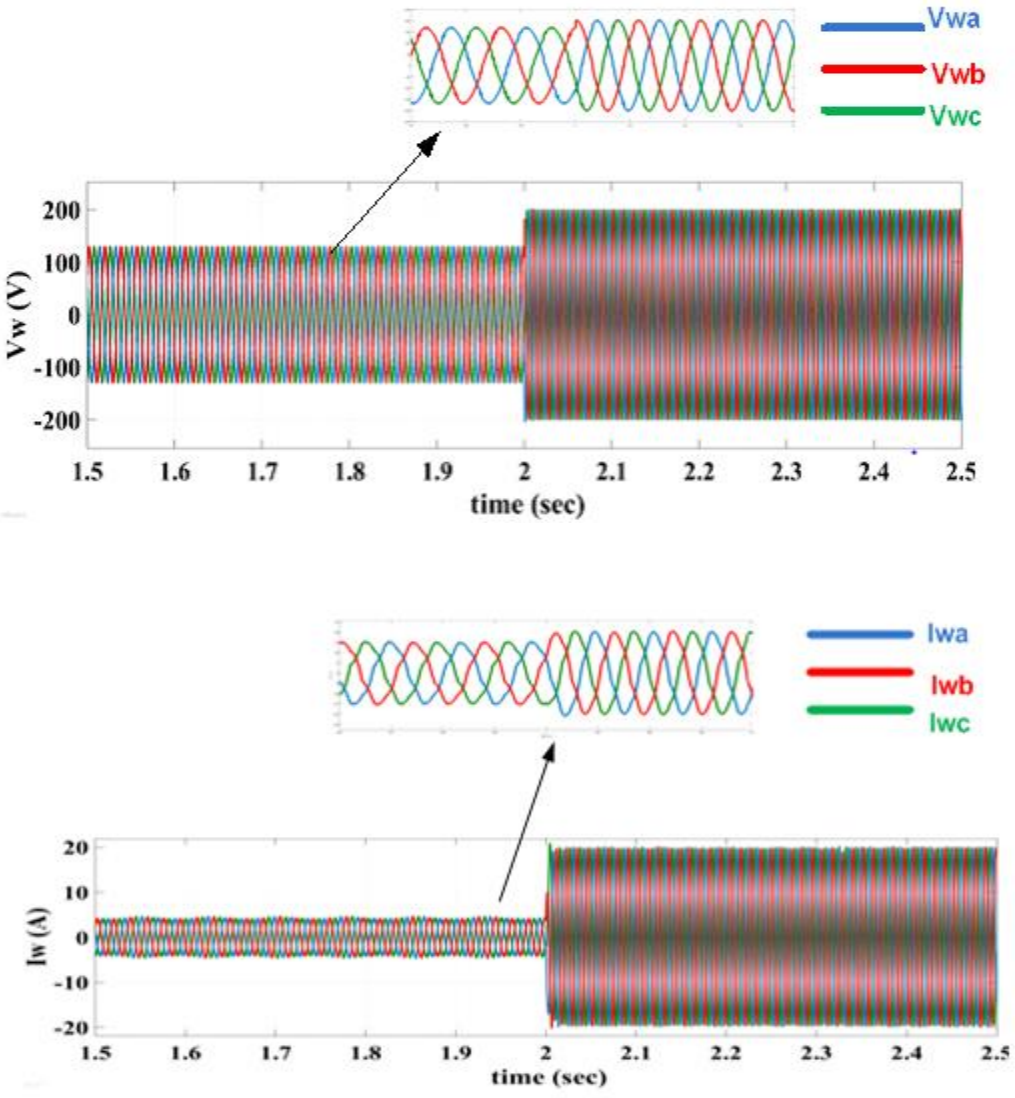

Fig. 15 Effects of PMSG voltage and currents at a rotor speed of 12 meters per second on SG performance.

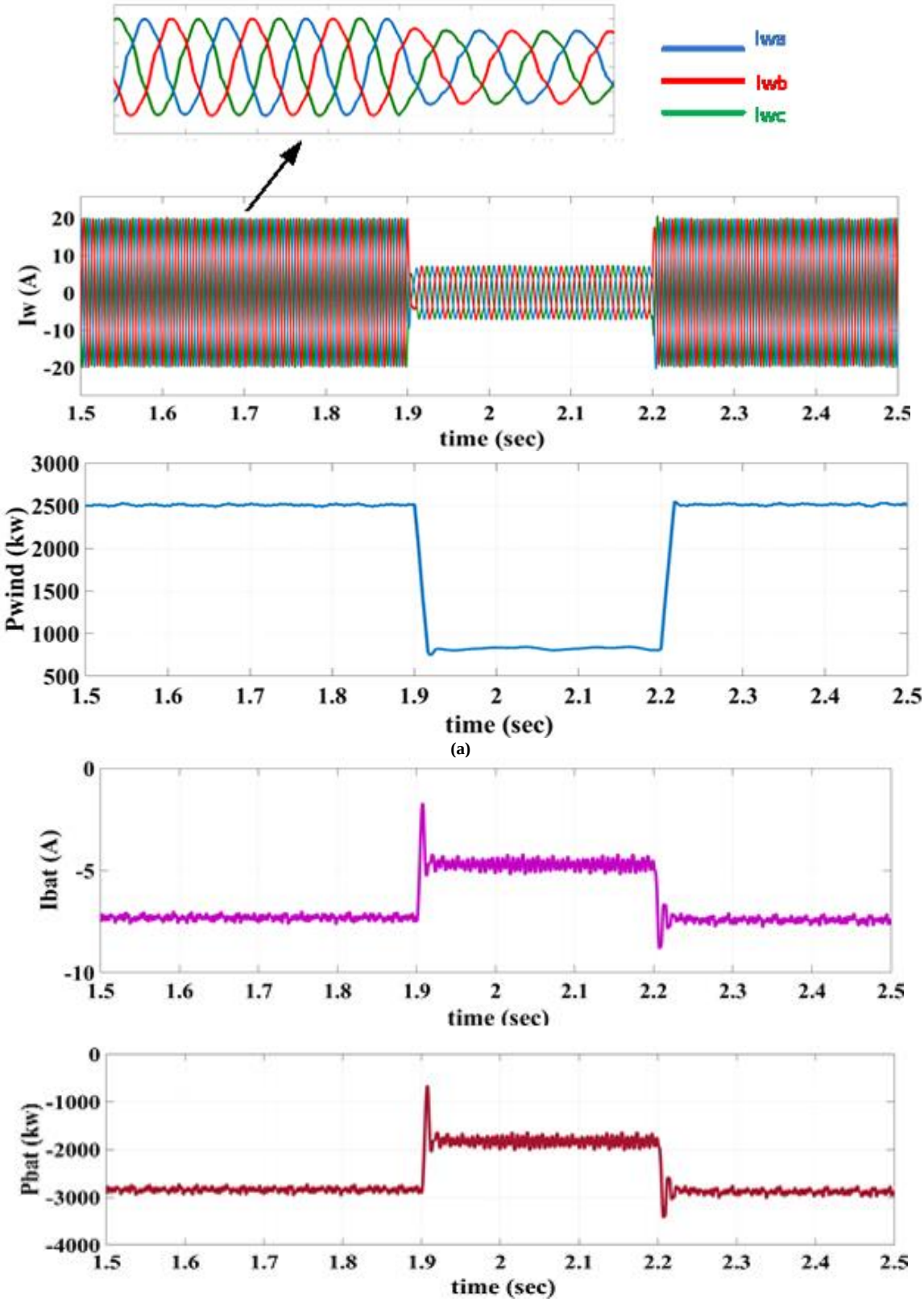
Iwa
Iwb
Iwc
Iw (A)
time (sec)
Pwind (kw)
time (sec)
Ibat (A)
time (sec)
Pbat (kw)
time (sec)

(a)

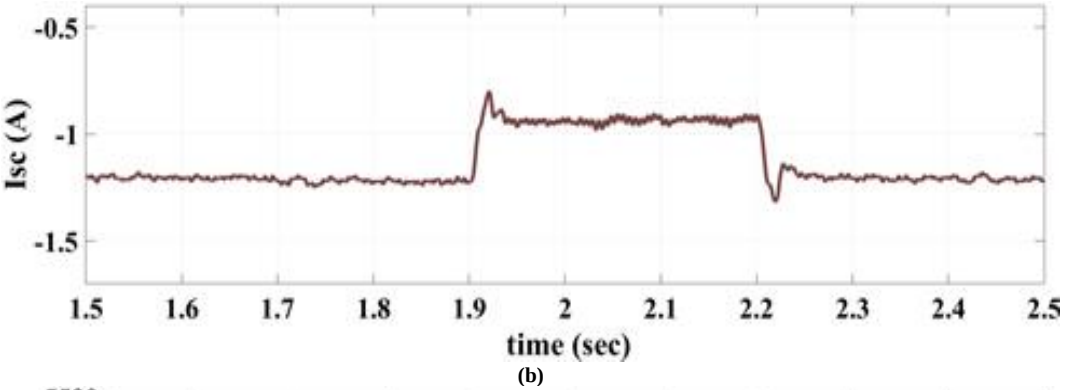
Isc (A)
-0.5
-1
-1.5
1.5 1.6 1.7 1.8 1.9 2 2.1 2.2 2.3 2.4 2.5
time (sec)

(b)

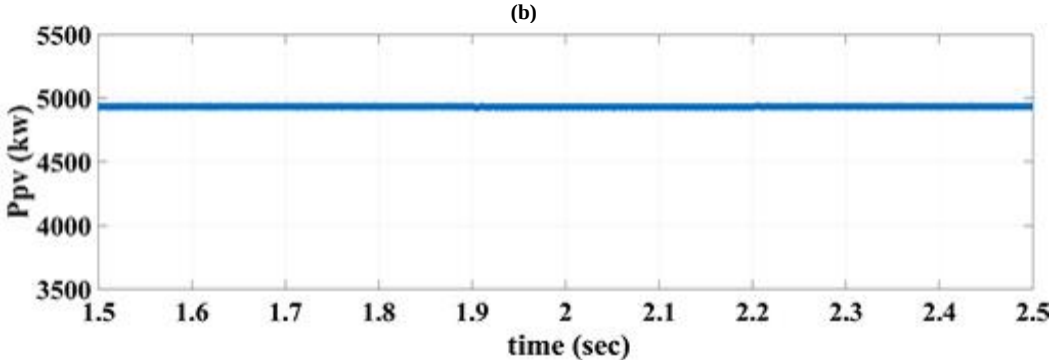
Ppv (kw)
5500
5000
4500
4000
3500
1.5 1.6 1.7 1.8 1.9 2 2.1 2.2 2.3 2.4 2.5
time (sec)

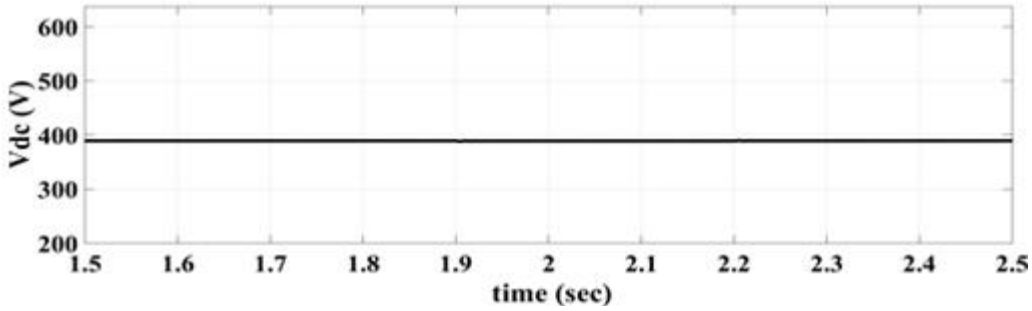
Vdc (V)
600
500
400
300
200
1.5 1.6 1.7 1.8 1.9 2 2.1 2.2 2.3 2.4 2.5
time (sec)

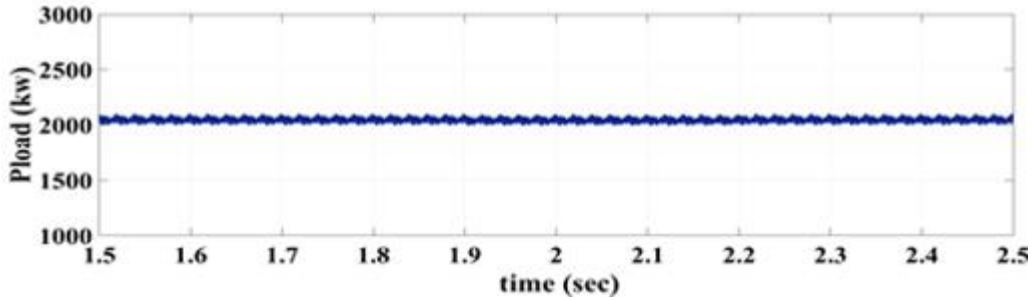
Pload (kw)
3000
2500
2000
1500
1000
1.5 1.6 1.7 1.8 1.9 2 2.1 2.2 2.3 2.4 2.5
time (sec)

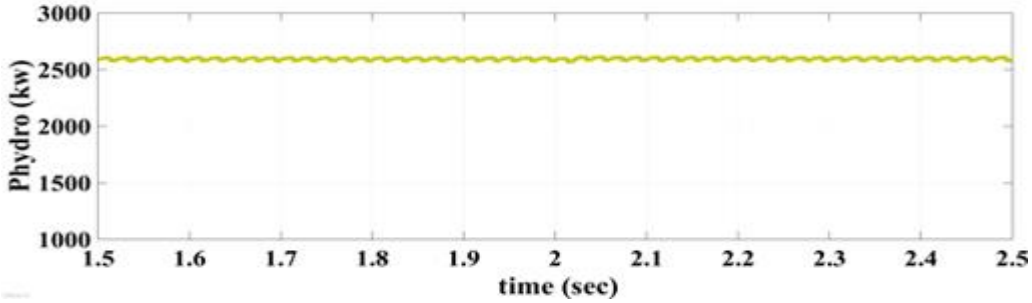
Phydro (kw)
3000
2500
2000
1500
1000
1.5 1.6 1.7 1.8 1.9 2 2.1 2.2 2.3 2.4 2.5
time (sec)

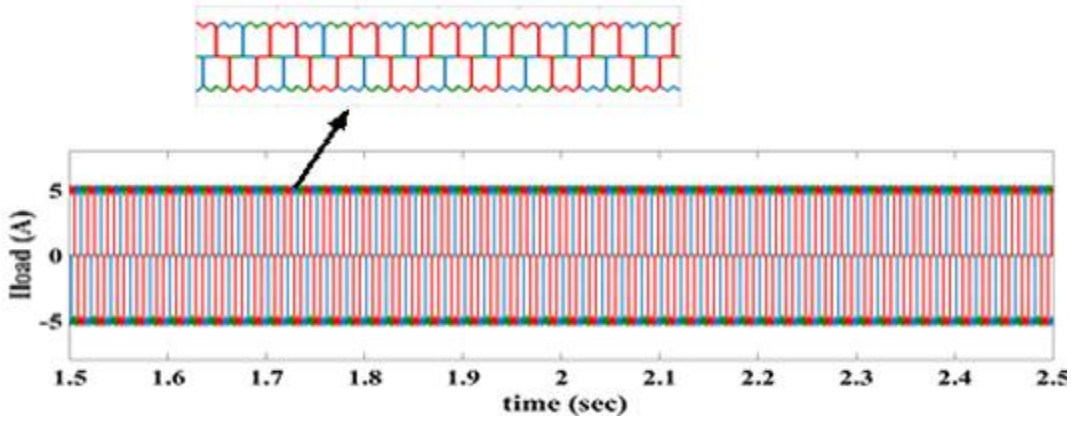

(c)

Fig. 16 (a) PMSG current and wind power variation during wind speed variability, (b-c) Load current, battery current, battery power, super capacitor current, solar power, Vdc, Load power, IAG power variation with wind speed variability.

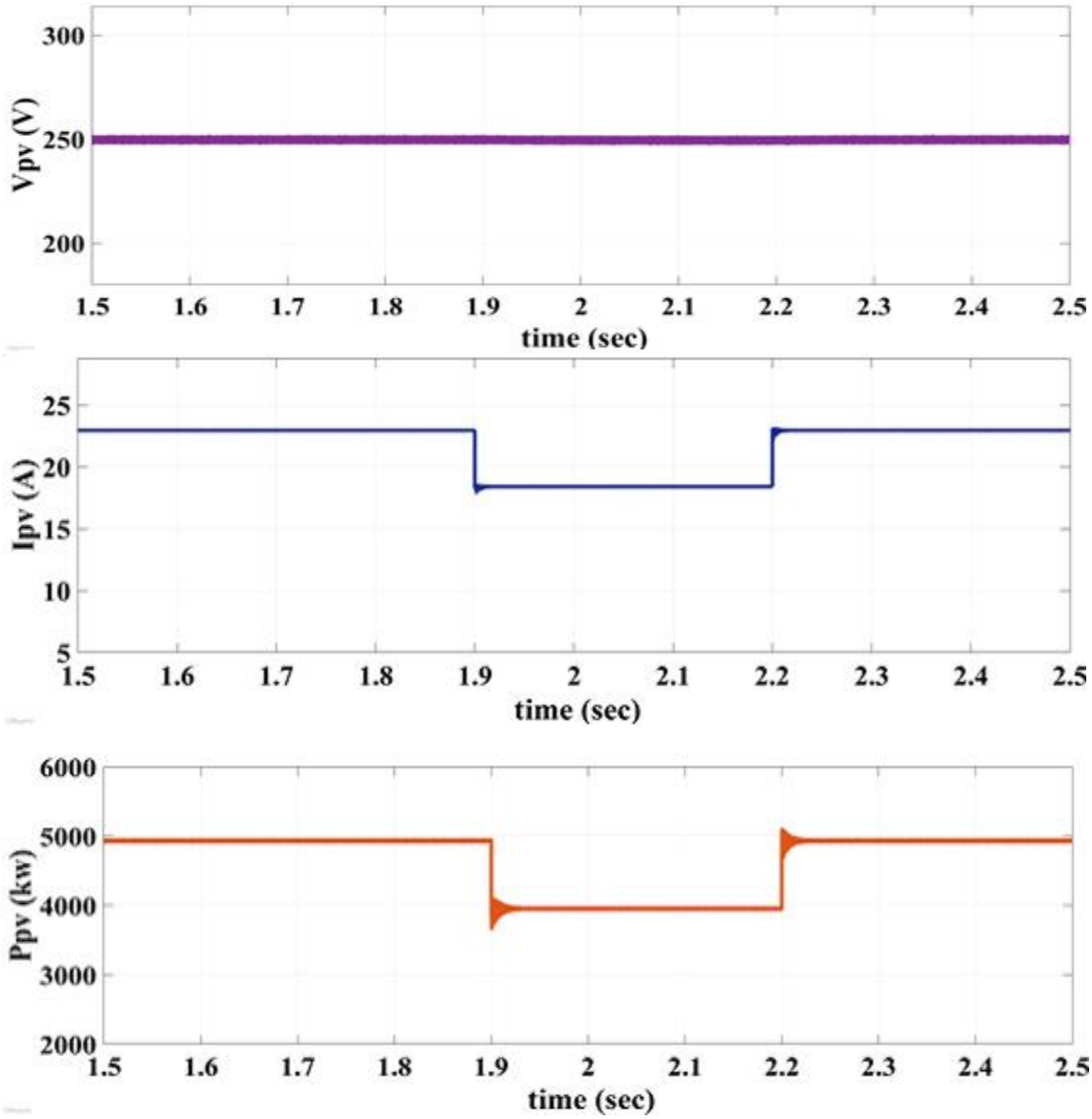

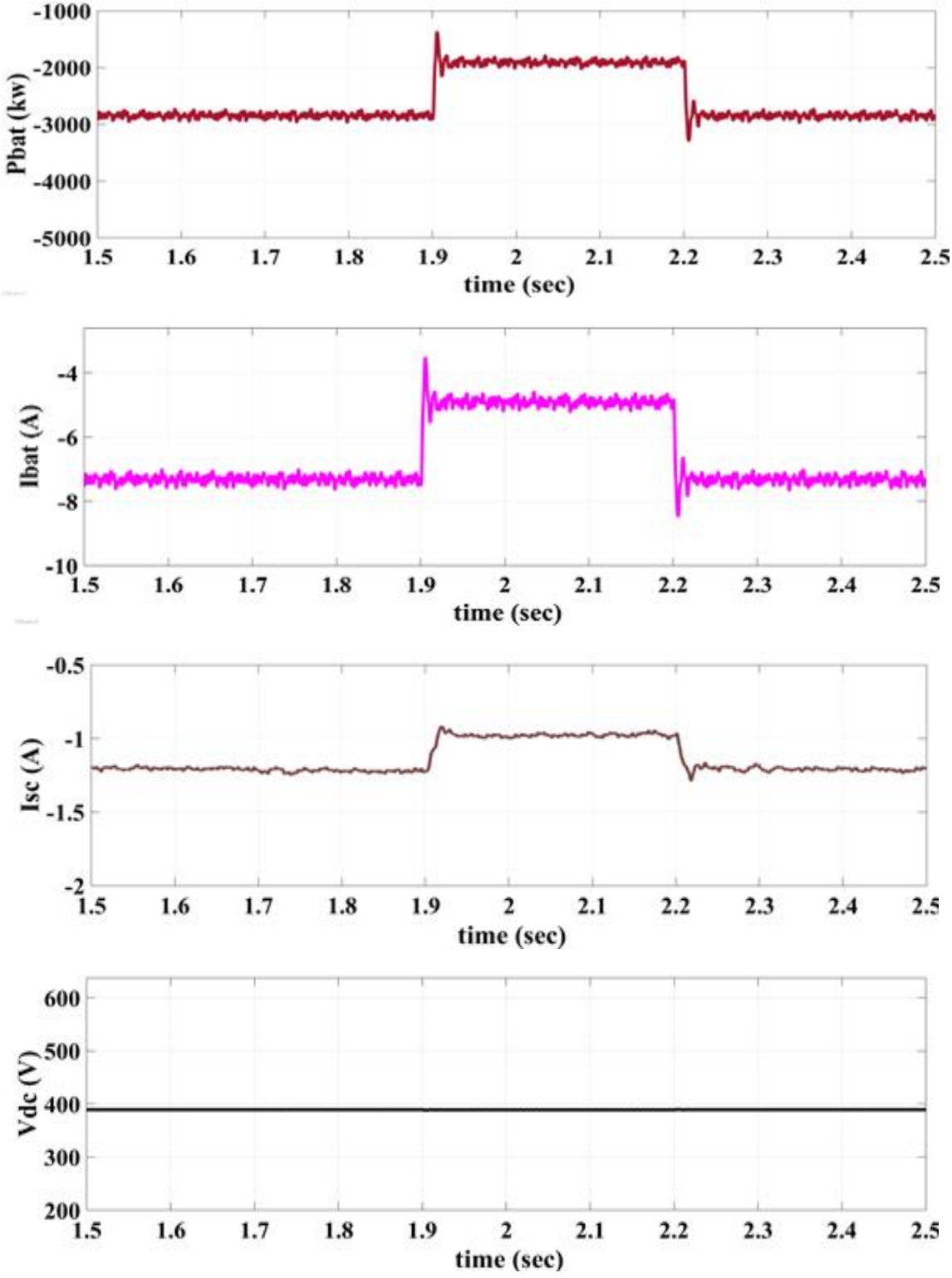
Pbat (kw)
-1000
-2000
-3000
-4000
-5000
1.5 1.6 1.7 1.8 1.9 2 2.1 2.2 2.3 2.4 2.5
time (sec)
Ibat (A)
-4
-6
-8
-10
1.5 1.6 1.7 1.8 1.9 2 2.1 2.2 2.3 2.4 2.5
time (sec)
Isc (A)
-0.5
-1
-1.5
-2
1.5 1.6 1.7 1.8 1.9 2 2.1 2.2 2.3 2.4 2.5
time (sec)
Vdc (V)
600
500
400
300
200
1.5 1.6 1.7 1.8 1.9 2 2.1 2.2 2.3 2.4 2.5
time (sec)

(a)

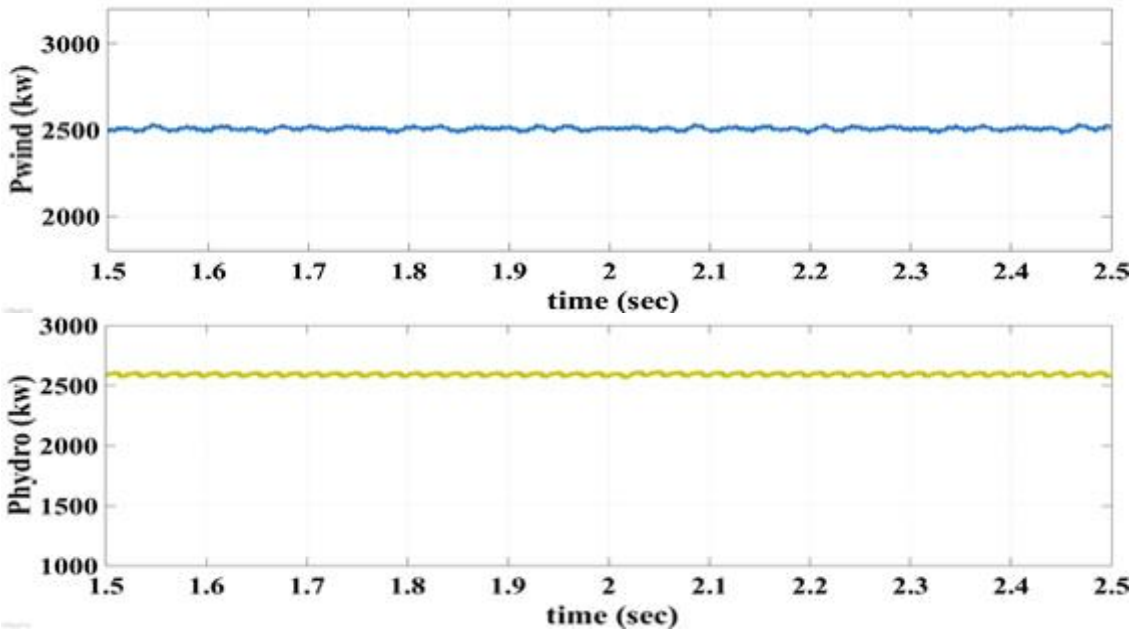

(b)

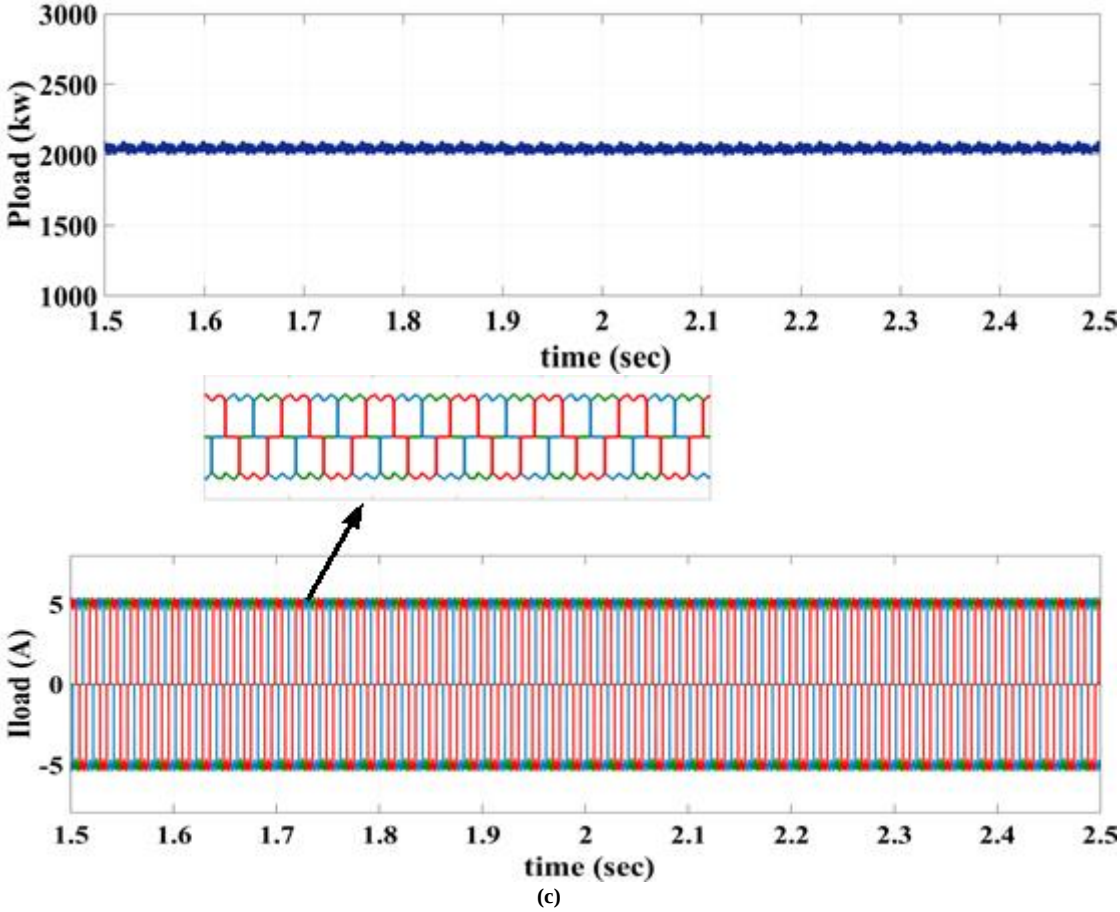

(c)

Fig. 17 (a) PV voltage, current, PV power, battery current, battery power, super capacitor current, Vdc variation during solar irradiation, (b) IAG power and wind power (c) Load current, Load power, variation with solar irradiation.

9.3 Behavior at Variability in Solar Insolation

Solar PV arrays can produce less electricity at t = 1.9s and 2.2s, but the battery and supercapacitor connected to the DC link keep the DC link voltage at the same level. It can be seen in Fig. 17 of the text (a). At full power, the hybrid system reduces the amount of insolation and generates electricity. When this is not enough to meet a load, the battery and supercapacitor are discharged to meet the load. As shown in Fig. 17, the battery and supercapacitor have stored charge, which is used to meet the load demand (c). The maximum amount of wind and IAG generation is found, and this is done. This is how it works: The combined power generation meets the needs of the loads, and any extra power goes to the loads, as shown in Fig. 17. (b).

9.4. Behavior at hydro speed Variability

In Fig. 18, you can see how hydro-based HRES performs in various ways (a-b). Phydro, the hydro system power, is also less at times when there is less speed in the hydro system (t = 1.9s and t = 2.2s). When less hydropower is discharged into the storage system by supercapacitor (Isc), battery charging current (Ibt), and battery power. The load demand (PL), wind generation (Pwind), and PV power are all the same (Pbt). The voltages (vabc) of the PCC stay the same, and the hydro currents (iabc) of the HRES are less. Currents in VSI compensate for reactive power demand change to keep voltages and currents balanced at the PCC and to remove harmonics. For the battery to keep up with everything, it needs to keep making HRES all the time. It shows that when things go wrong, HRES gives a good answer.

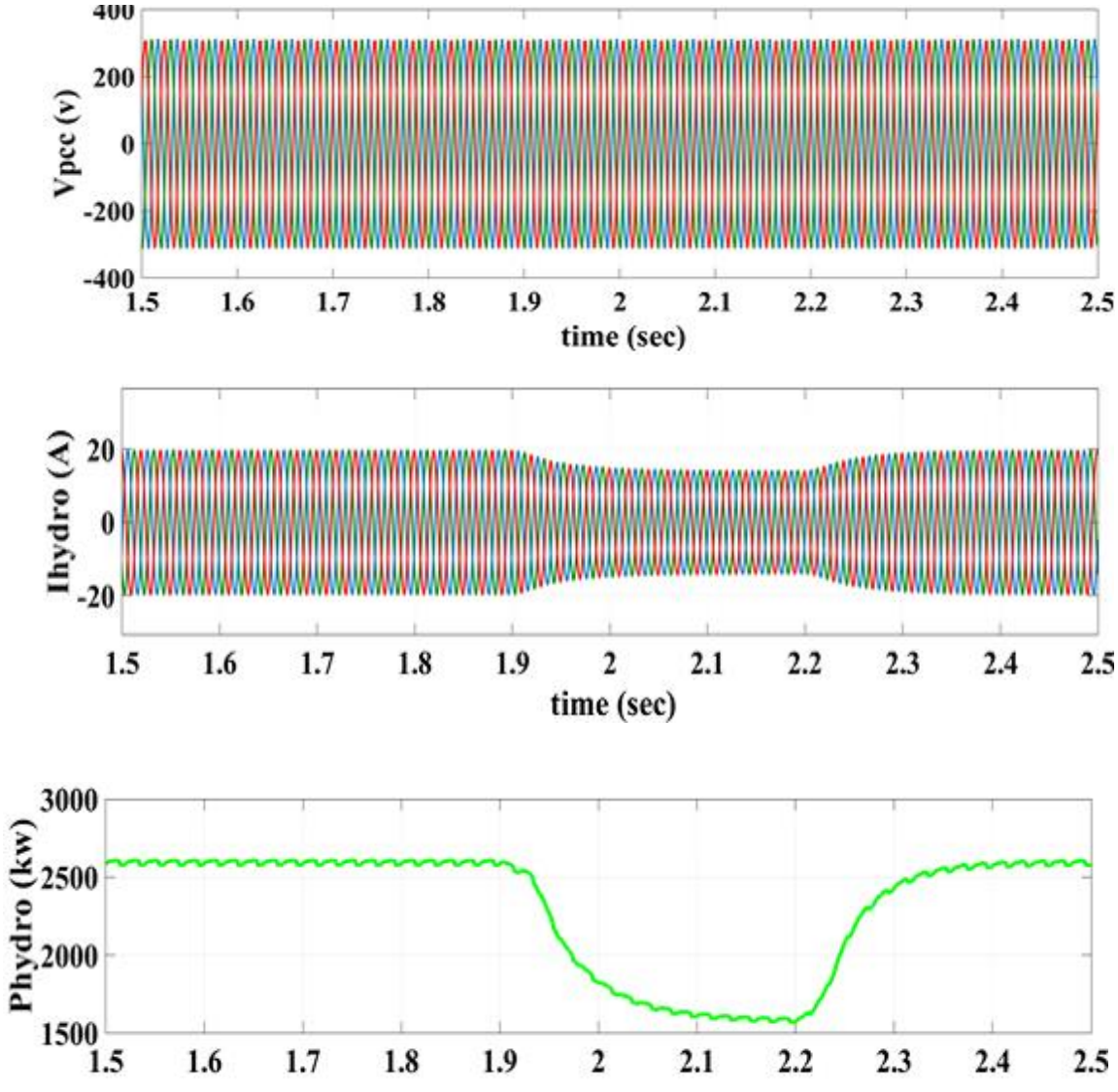

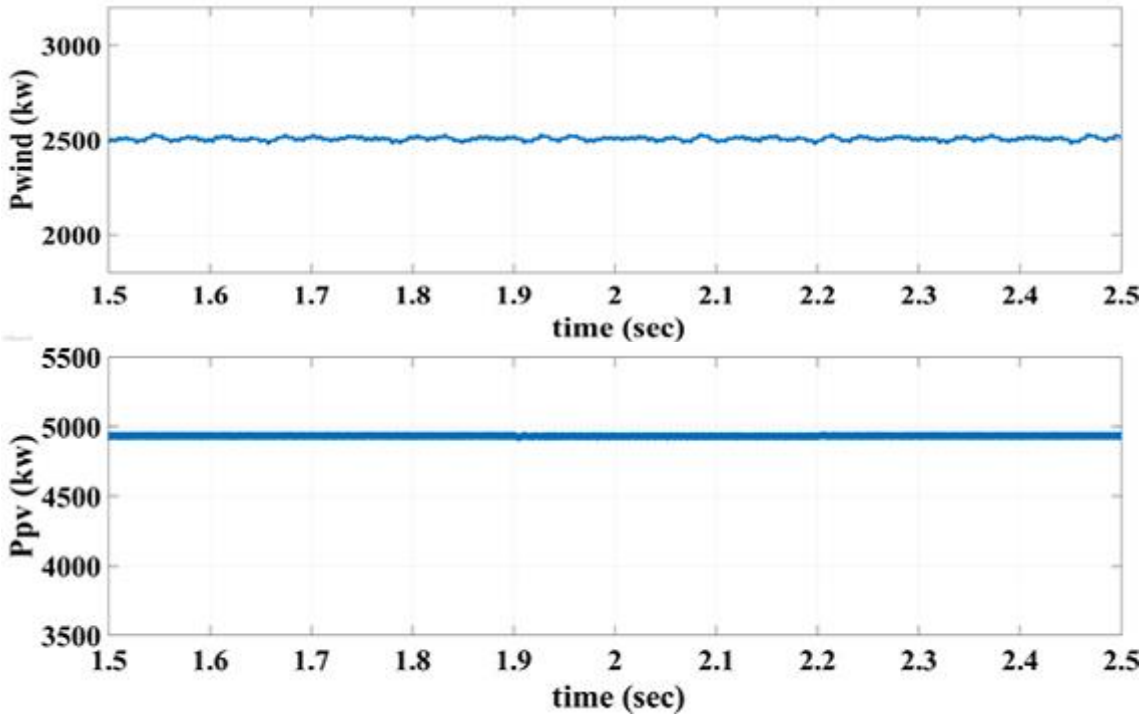
Pwind (kw)
3000
2500
2000
1.5 1.6 1.7 1.8 1.9 2 2.1 2.2 2.3 2.4 2.5
time (sec)
Ppv (kw)
5500
5000
4500
4000
3500
1.5 1.6 1.7 1.8 1.9 2 2.1 2.2 2.3 2.4 2.5
time (sec)

(a)

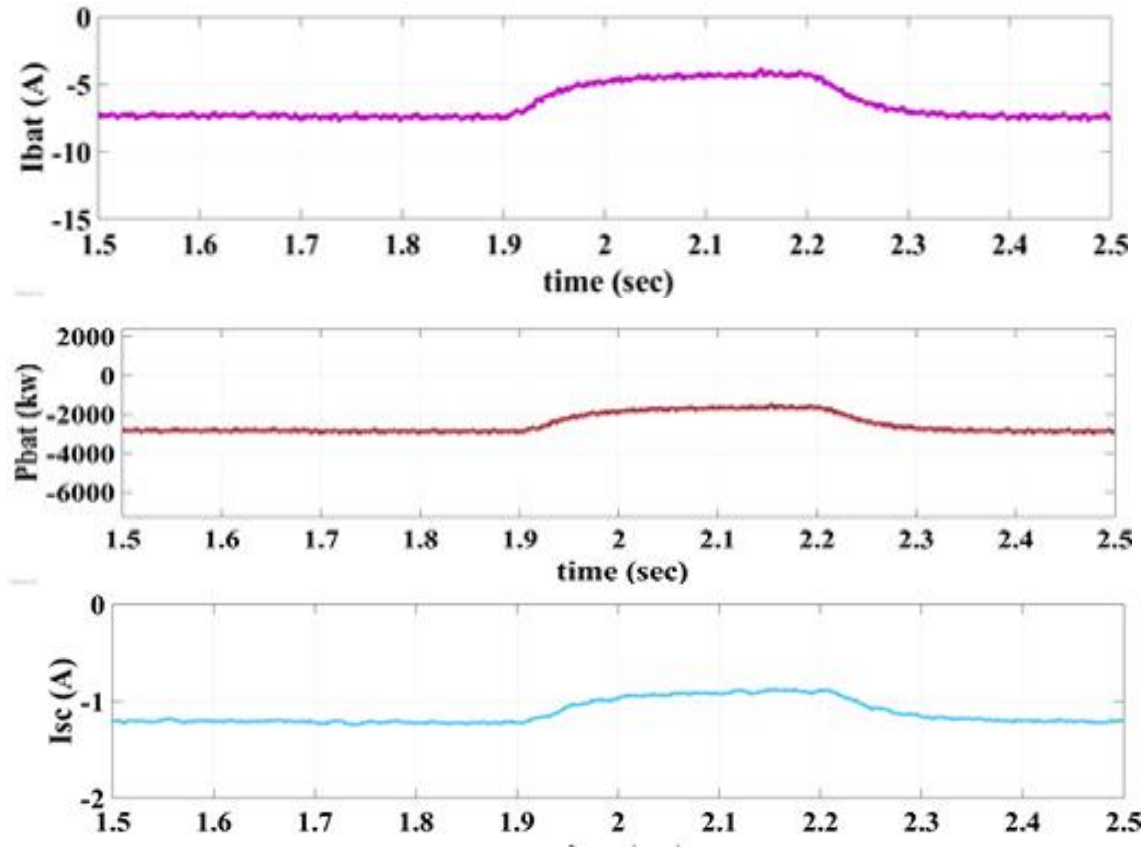
Ibat (A)
0
-5
-10
-15
1.5 1.6 1.7 1.8 1.9 2 2.1 2.2 2.3 2.4 2.5
time (sec)
Pbat (kw)
2000
0
-2000
-4000
-6000
1.5 1.6 1.7 1.8 1.9 2 2.1 2.2 2.3 2.4 2.5
time (sec)
Isc (A)
0
-1
-2
1.5 1.6 1.7 1.8 1.9 2 2.1 2.2 2.3 2.4 2.5

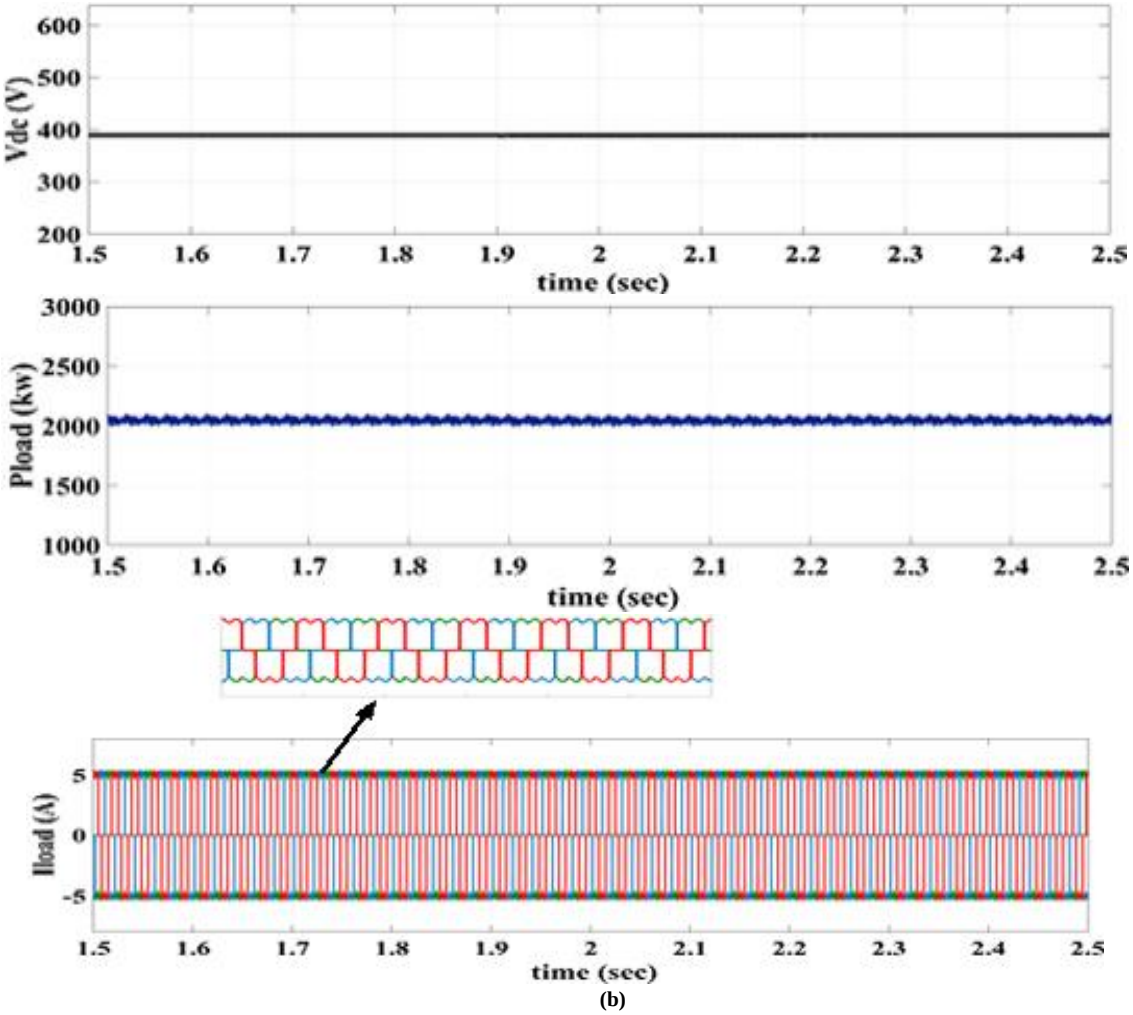

(b)

Fig. 18 (a-b) PCC voltage, IAG current and hydropower variation during IAG speed variability, (b) Load current, battery current, battery power, super capacitor current, Vdc, Load power, IAG power and wind power variation with IAG speed variability.

9.5. Behavior at Variability in Load Variation

1.9s and 2.2s have the same hybrid system difficulties. The hybrid system in this work satisfies all load demands. Fig. 19 (a) demonstrates what happens when solar, wind, and hydropower are at total capacity and the demand is off. At this moment, battery charging (negative increase) begins. It stores the energy made, which can be used in the way the person needs. Fig. 19 (b) graph shows how much power each energy source gives off. It shows how much power each source of energy gives off. Unexpectedly, a load is cut off. Because the power consumed by the load is now rendered useless, it is transferred to the battery to be stored there. Since the battery's power increases, the result is:

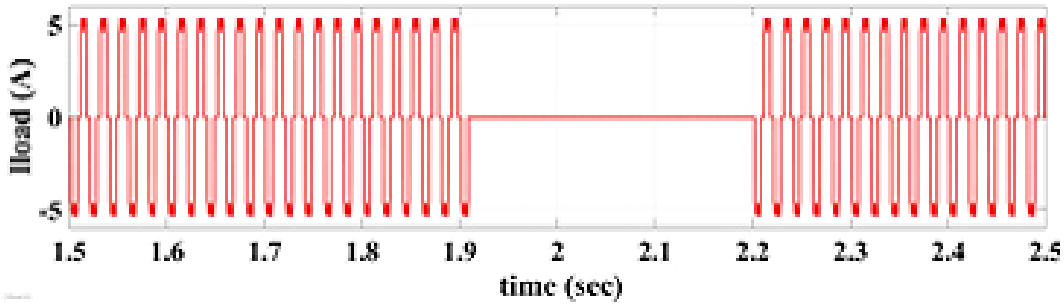

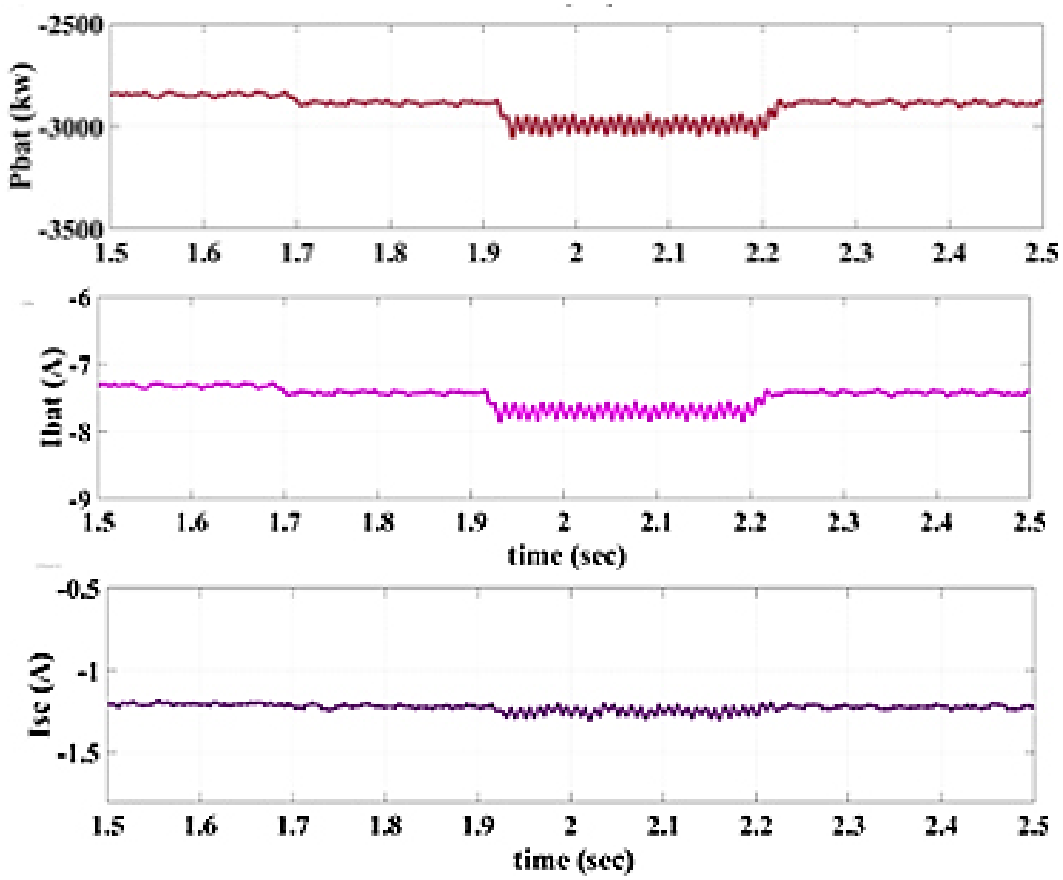
Pbat (kw)
-2500
-3000
-3500
Ibat (A)
-6
-7
-8
-9
Isc (A)
-0.5
-1
-1.5
1.5 1.6 1.7 1.8 1.9 2 2.1 2.2 2.3 2.4 2.5
time (sec)

(a)

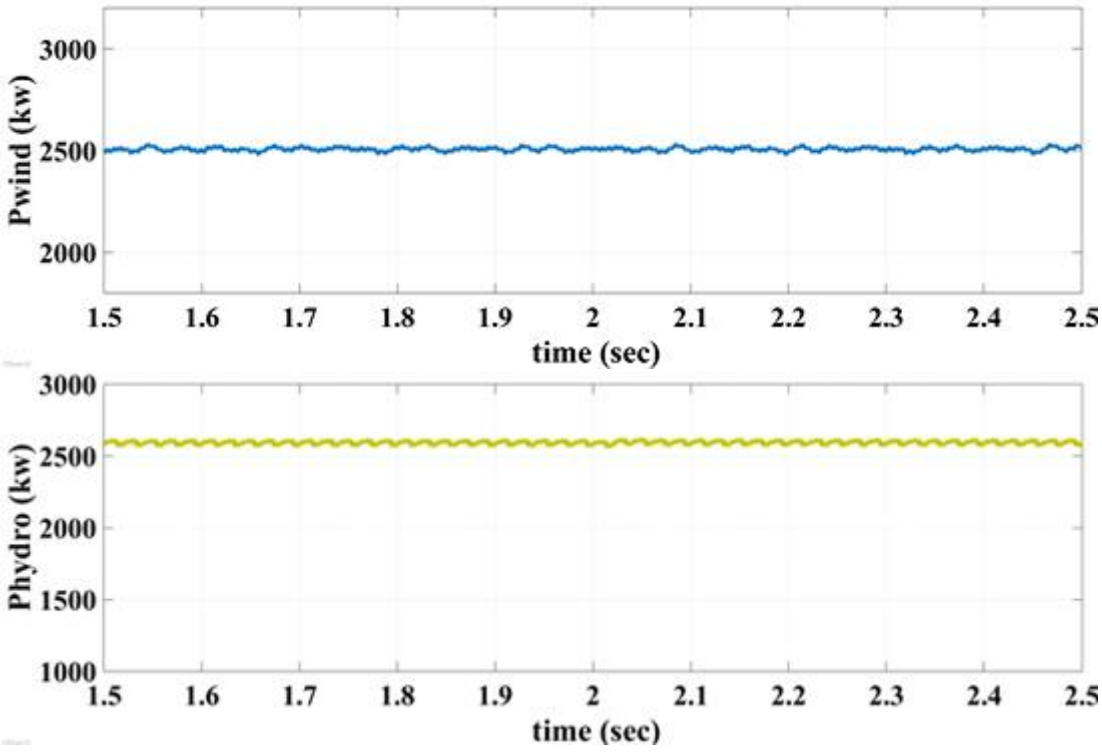
Pwind (kw)
3000
2500
2000
Phydro (kw)
3000
2500
2000
1500
1000
1.5 1.6 1.7 1.8 1.9 2 2.1 2.2 2.3 2.4 2.5
time (sec)

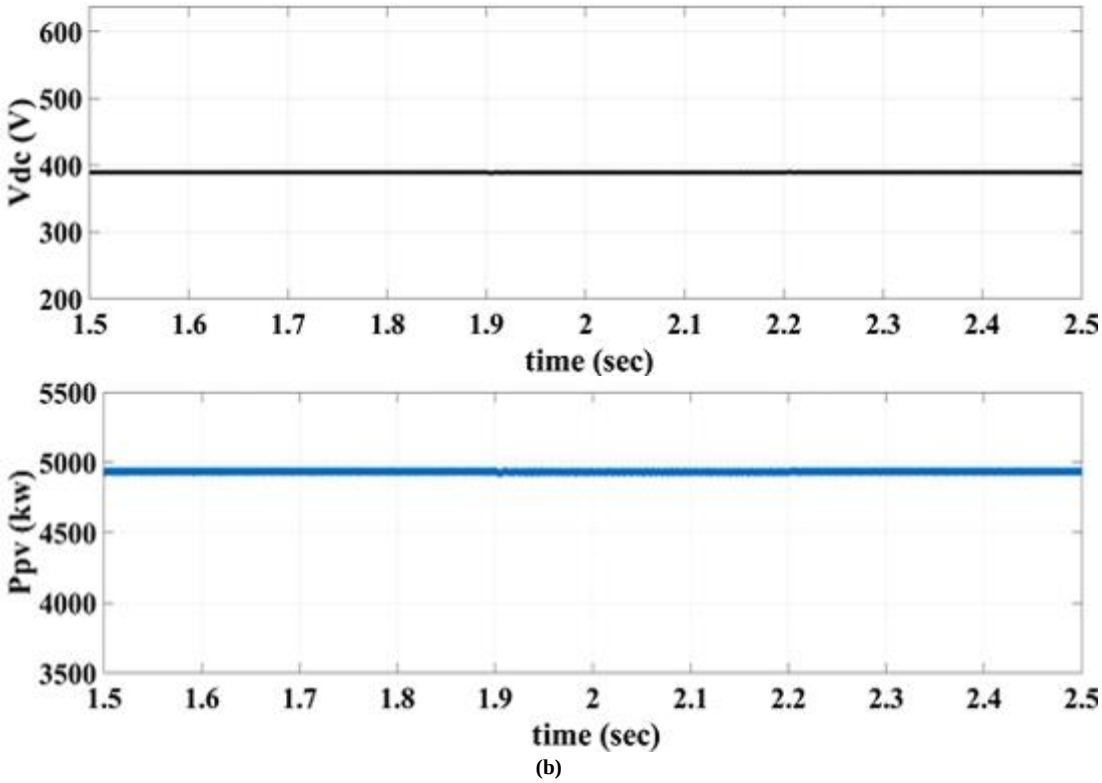

(b)

Fig. 19 (a-b) Performance of Load current, battery power, battery current, super capacitor current, wind power, solar power, IAG hydro system power, Vdc dc link voltage during load disconnection and simultaneous power variations.

9.6. Power Fluctuations in Hybrid Systems Due to Renewable Energy's Unpredictability

Fig. 20 shows how the system works when there is much renewable energy in the system. Battery and supercapacitors are used when the solar array does not produce enough energy at t = 1.3s and t = 2.15s. The IAG hydro system and wind turbine-driven PMSG produce enough energy to meet the demand. During low wind speeds at t = 1.25 s and t = 2.3 s, the wind does not produce enough energy, so the wind is considered zero. So it has to discharge the battery and supercapacitor to get the rated power from the solar array. This gets the power that they need to see what is going on. During the summer, when the hydro system does not produce enough electricity at times like t = 1.6s and t = 1.9s, the battery and supercapacitor discharge to meet the electricity demand. When there is not enough energy coming from wind and solar, the battery and supercapacitor discharge to meet the needs of the people who use the electricity, It looks like Fig. 20 when the combined performance is shown at times when t is 0.8 and t is 2.5 (a-b).

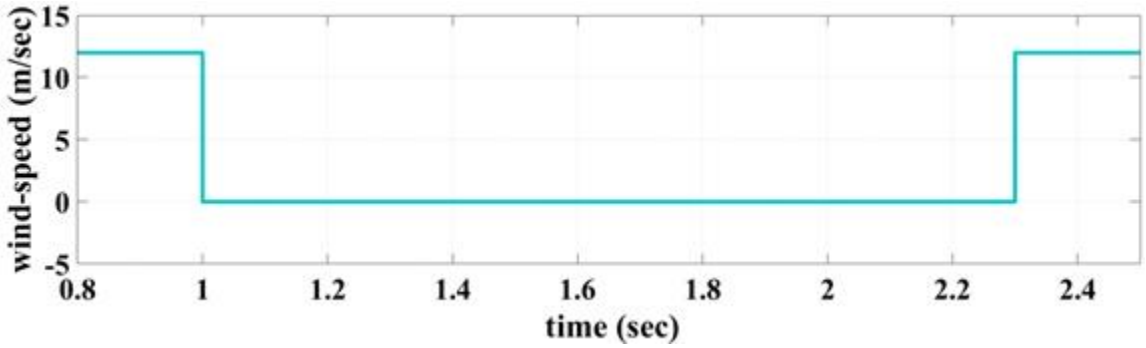

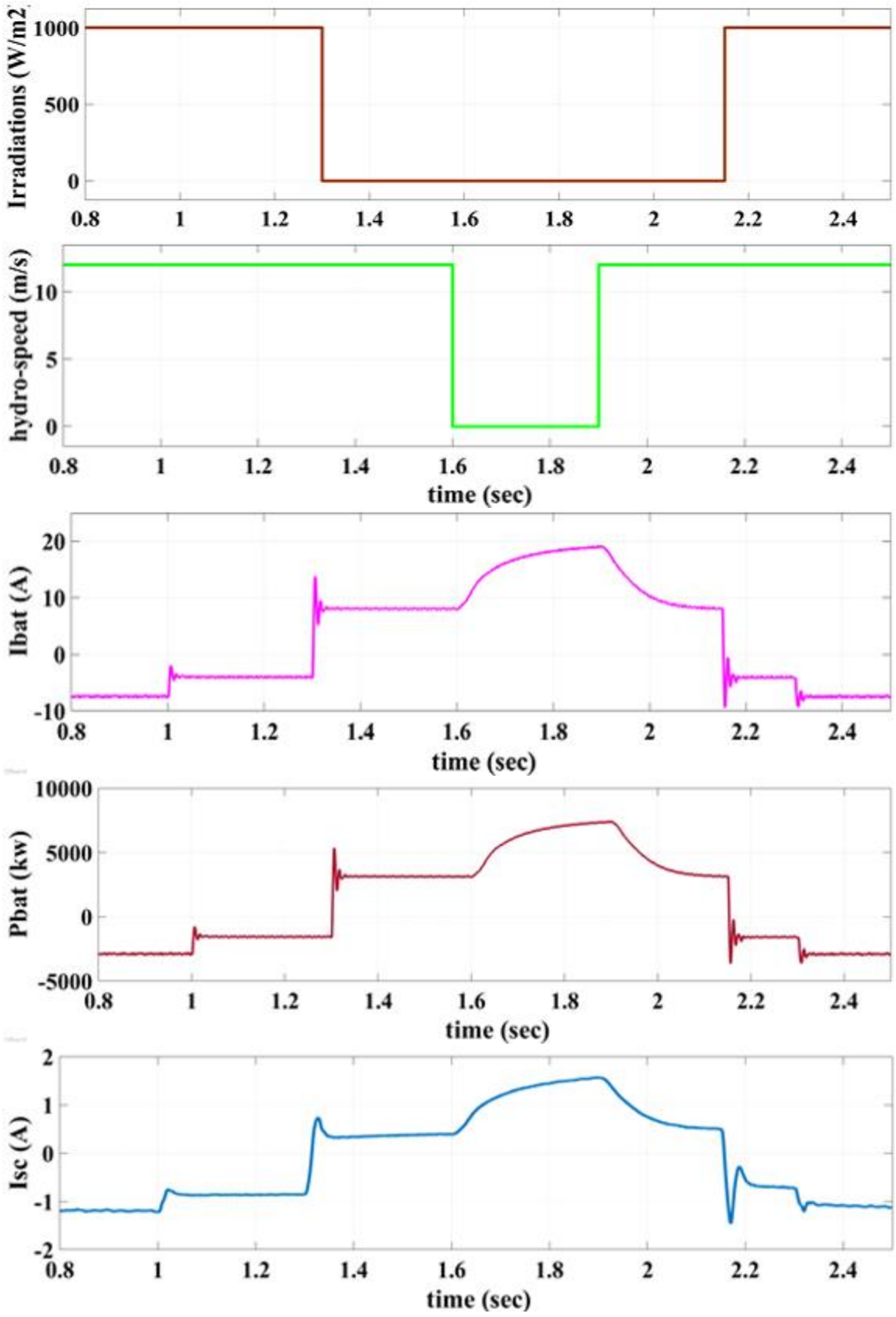
Irradiations (W/m2)
1000
500
0
0.8 1 1.2 1.4 1.6 1.8 2 2.2 2.4
hydro-speed (m/s)
10
5
0
0.8 1 1.2 1.4 1.6 1.8 2 2.2 2.4
time (sec)
Ibat (A)
20
10
0
-10
0.8 1 1.2 1.4 1.6 1.8 2 2.2 2.4
time (sec)
Pbat (kw)
10000
5000
0
-5000
0.8 1 1.2 1.4 1.6 1.8 2 2.2 2.4
time (sec)
Isc (A)
2
1
0
-1
-2
0.8 1 1.2 1.4 1.6 1.8 2 2.2 2.4
time (sec)

(a)

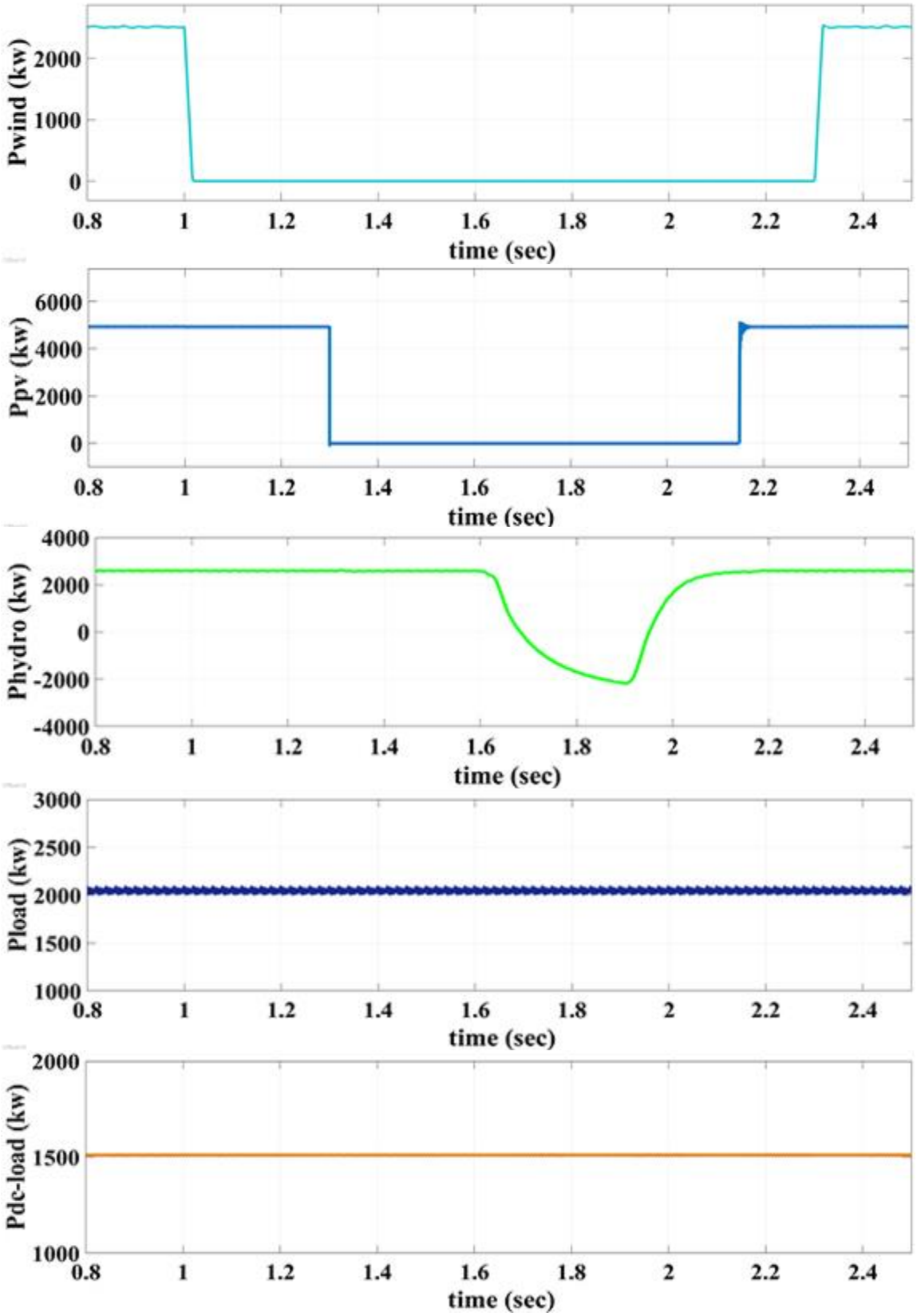
Pwind (kw)
2000
1000
0
0.8
1
1.2
1.4
1.6
1.8
2
2.2
2.4
time (sec)
Ppv (kw)
6000
4000
2000
0
time (sec)
Phydro (kw)
4000
2000
0
-2000
-4000
time (sec)
Pload (kw)
3000
2500
2000
1500
1000
time (sec)
Pdc-load (kw)
2000
1500
1000
time (sec)

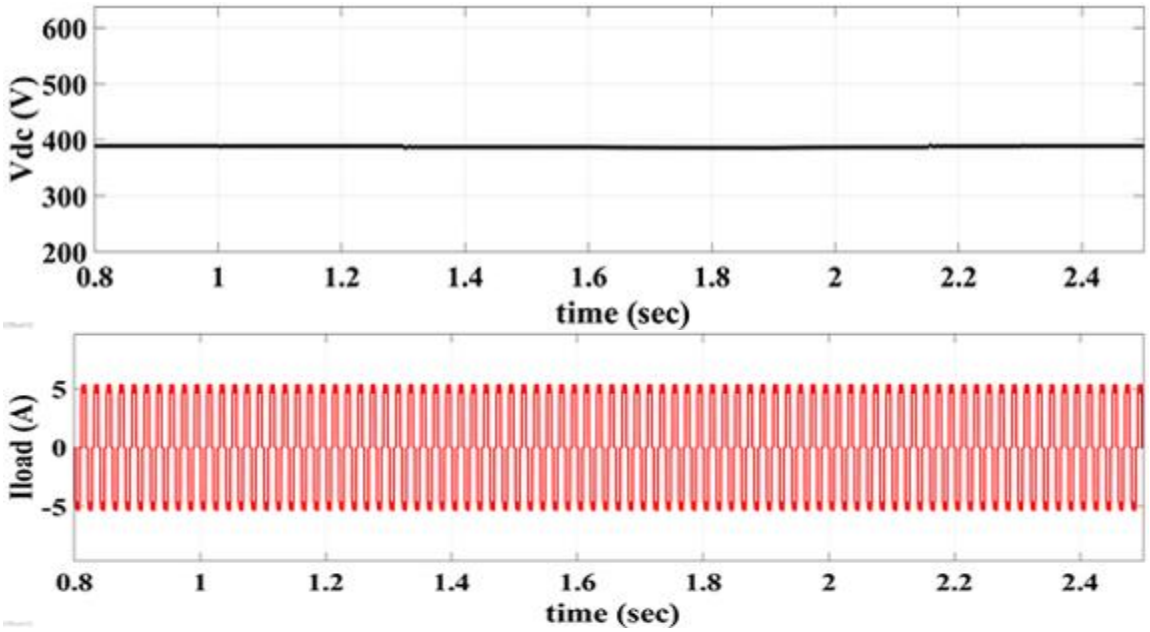

(b)

Fig. 20 (a-b) The performance of the PMSG power, Solar PV power, load power, and battery power components of an HRES in the face of fluctuating renewable generation

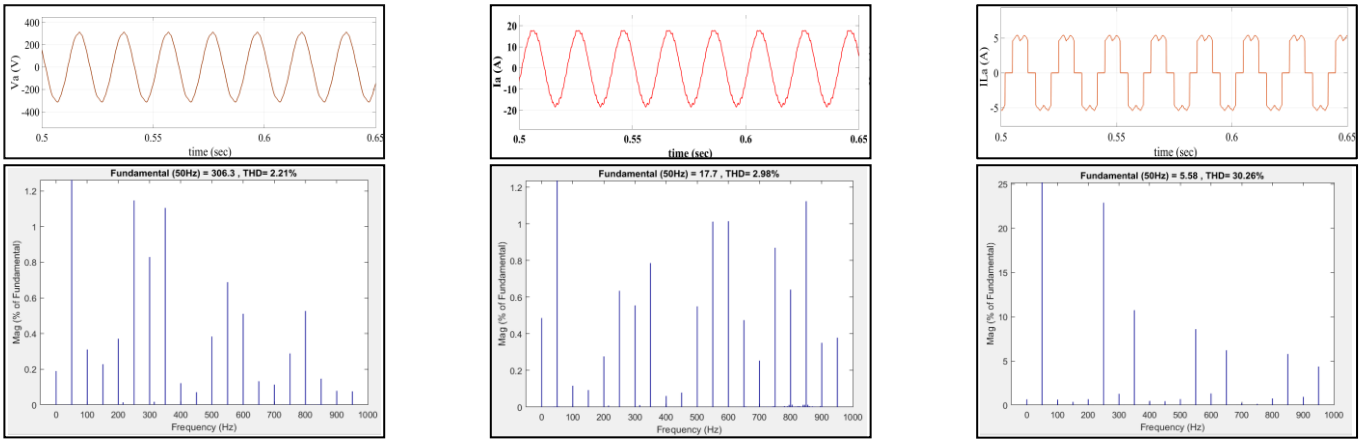

Fig. 21 Harmonic spectra of (a) generator voltage (*Va*), (b) generator current (*isa*), and (c) load current (*ila*) under Steady-State Condition.

9.7. Steady-State Condition

As shown in Fig. 21(a), the source-voltage waveform and its harmonic spectrum, which exhibits a total harmonic distortion (THD) of 2.21%, are depicted as waveforms. These waveforms are useful for monitoring steady-state operation. The total harmonic distortion (THD) is 2.98%, as shown in Fig. 21(b), indicating a great deal of background noise in the source current. The waveform and harmonic spectrum of nonlinear load current, depicted in Fig. 21(c), reveals a total harmonic distortion (THD) of 30.26%. The terminal voltage and current from the generator should have a THD of no more than 5%, as specified by IEEE-519 standard.

10. Conclusion

This paper presents and evaluates an ANFIS-based HRES that uses renewable energy sources (wind turbines and photovoltaic panels), storage, and control. Gasoline is more costly than renewable energy. Therefore, it drives up system costs. HRES use, scale, and annual cost can only be reduced. It was considered in the proposed energy management strategy. Simulation findings show more reliable power and less fuel consumption. MPPT's renewable energy sources operate independently of HRES. The HRES controls the ESS (battery and supercapacitor system) based on hydro, renewable, and ESS power needs (battery SOC and supercapacitor SOC). To keep the HRES's dc bus voltage stable, the ESS manages the dc-dc converter connected to the battery and supercapacitor system. An ANFIS-based controller and HRES manage the hybrid system's active and reactive power. Both HRES can provide the required energy to the hydro-producing system, maintaining battery and supercapacitor SOC within limits. The ANFIS-based HRES

has superior battery and supercapacitor hybrid system efficiencies and energy injection capacity. Short-scale operation exhibits dc bus voltage and three-phase inverter output voltage and current to illustrate the hybrid system's accurate dynamic reactivity to rapid power fluctuations.

References

[1] Liu Jizhen, "Basic Issues of the Utilization of Large-Scale Renewable Power with High Security and Efficiency," *Proceedings of the Chinese Society of Electrical Engineering*, vol. 33, no. 16, pp. 1-8, 2013.

[2] Ntomaris A V, Bakirtzis A G, "Stochastic Scheduling of Hybrid Power Stations in Insular Power Systems with High Wind Penetration," *IEEE Transactions on Power Systems*, vol. 31, no. 5, pp. 3421-3436, 2016. Crossref, http://doi.org/10.1109/TPWRS.2015.2499039

[3] Morales-España G, Baldick R, García-González J and Ramos A, "Power-Capacity and Ramp-Capability Reserves for Wind Integration in Power-Based UC," *IEEE Transactions on Sustainable Energy*, vol. 7, no. 2, pp. 614-624, 2016. Crossref, http://doi.org/10.1109/TSTE.2015.2498399

[4] J. B. Ekanayake, "Induction Generators for Small Hydro Schemes," *Power Engineering Journal*, vol. 16, no. 2, pp. 61–67, 2002. Crossref, http://doi.org/10.1049/pe:20020202

[5] J. Bjornstedt and O. Samuelsson, "Voltage and Frequency Control for Island Operated Induction Generators," *In Proceedings of IET CIRED Smart Hydro Generators Distribution*, pp. 1-4, 2008. Crossref, http://doi.org/10.1049/ic:20080484

[6] Vanam Satyanarayana, and Vairavasamy Jayasankar, "Advanced Modeling and Optimization of Hybrid Renewable Energy Management Strategy Based on Artificial Bee Colony Algorithm in Micro Grid," *International Journal of Engineering Trends and Technology*, vol. 70, no. 10, pp. 329-338, 2022. Crossref, https://doi.org/10.14445/22315381/IJETT-V70I10P232

[7] Y. Zidani and M. Naciri, "A Numerical Analytical Approach for the Optimal Capacitor Used for the Self-Excited Induction Generator," *In 2001 IEEE 32nd Annual Power Electronics Specialists Conference*, vol. 1, pp. 216–220, 2001. Crossref, https://doi.org/10.1109/PESC.2001.954022

[8] B. Singh, G. K. Kasal, and S. Gairola, "Power Quality Improvement in Conventional Electronic Load Controller for an Isolated Power Generation," *IEEE Transactions on Energy Conversion*, vol. 23, no. 3, pp. 764–773, 2008. Crossref, https://doi.org/10.1109/TEC.2008.921481

[9] Y.Liu, S.Tan, and C.Jiang, "Interval Optimal Scheduling of Hydro-PV-Wind Hybrid System Considering Firm Generation Coordination," *IET Renewable Power Generation*, vol. 11, no. 1, pp. 63-72, 2017. Crossref, https://doi.org/10.1049/iet-rpg.2016.0152

[10] XU Fei, Chen Lei. Jin Heping, "Modeling and Application of Joint Optimal Operation of Pumped Storage Power Station and Wind Power," *Electric Power System and Automation*, vol. 37, no. 1, pp. 149-154, 2013.

[11] S. P. Singh, B. Singh, and M. P. Jain, "Performance Characteristics and Optimum Utilization of a Cage Machine as Capacitance Excited Induction Generator," *IEEE Transactions on Energy Conversion*, vol. 5, no. 4, pp. 679–685, 1990. Crossref, https://doi.org/10.1109/60.63139

[12] B. Singh, S. S. Murthy, and S. Gupta, "Analysis and Design of STATCOM Based Voltage Regulator for Self-Excited Induction Generators," *IEEE Transactions on Energy Conversion*, vol. 19, no. 4, pp. 783–790, 2004. Crossref, https://doi.org/10.1109/TEC.2004.827710

[13] A. K. Abdelsalam, A. M. Massoud, S. Ahmed, and P. Enjeti, "Highperformance Adaptive Perturb and Observe MPPT Technique for Photovoltaic-Based Hybrid Systems," *IEEE Transactions on Power Electronics*, vol. 26, no. 4, pp. 1010–1021, 2011. Crossref, https://doi.org/10.1109/TPEL.2011.2106221

[14] Abdullah M.A, Yatim A.H.M, Tan C.W, Saidur R, "A Review of Maximum Power Point Tracking Algorithms for Wind Energy Systems," *Renewable and Sustainable Energy Reviews*, vol. 16, pp. 3220– 3227, 2012. Crossref, https://doi.org/10.1016/j.rser.2012.02.016

[15] G. Srinivasa Rao, K.V. Sharma, "Numerical and Experimental Investigation of a Packed bed Thermal Energy Storage System with Hybrid Nanofluid," *SSRG International Journal of Mechanical Engineering*, vol. 5, no. 1, pp. 19-25, 2018. Crossref, https://doi.org/10.14445/23488360/IJME-V5I1P104

[16] A. Gift IssacȦ, P. K. Senthil Kumara, "Fuzzy Adaptive Internal Model control for the Speed Regulation of a Permanent Magnet Synchronous Motor with an Index Matrix Converter," *International Journal of Current Engineering and Technology*, pp. 1324-1330, 2014.

[17] Abdullah M.A, Yatim A.H.M, Tan C.W, and Saidur R, "A Review of Maximum Power Point Tracking Algorithms for Wind Energy Systems," *Renewable and Sustainable Energy Reviews*, vol. 16, no. 5, pp. 3220– 3227, 2012. Crossref, https://doi.org/10.1016/j.rser.2012.02.016

[18] A. Berrueta, I. S. Martín, P. Sanchis and A. Ursúa, "Comparison of State-of-Charge Estimation Methods for Stationary Lithium-Ion Batteries," *IECON 2016 - 42nd Annual Conference of the IEEE Industrial Electronics Society*, Florence, pp. 2010-2015, 2016. Crossref, https://doi.org/10.1109/IECON.2016.7794094

[19] A. Khaligh and Z. Li, "Battery, Ultracapacitor, Fuel Cell, and Hybrid Energy Storage Systems for Electric, Hybrid Electric, Fuel Cell, and Plugin Hybrid Electric Vehicles: State of the Art," *IEEE Transactions on Vehicular Technology*, vol. 59, no. 6, pp. 2806–2814, 2010. Crossref, https://doi.org/10.1109/TVT.2010.2047877

[20] W. Jing, C. Hung Lai, S. H. W. Wong, and M. L. D. Wong, "Batterysupercapacitor Hybrid Energy Storage System in Stand-Alone Dc Microgrids: A Review," *IET Renewable Power Generation*, vol. 11, no. 4, pp. 461–469, 2017. Crossref, https://doi.org/10.1049/ietrpg. 2016.0500,

[21] R Sivapriyan, Sakshi N, C V Mohan, Lavan Raj, "Comprehensive Review on State of Charge Estimation in Battery Management System" *International Journal of Engineering Trends and Technology*, vol. 70, no. 7, pp. 169-179, 2022.

Crossref, https://doi.org/10.14445/22315381/IJETT-V70I7P218

[22] Ahmad Al-Sarraj, Hussein T. Salloom, Kareem K.Mohammad, Saad M.Mohammadghareeb, "Simulation Design of hybrid System (Grid/PV/Wind Turbine/ battery /diesel) with applying HOMER: A case study in Baghdad, Iraq," *SSRG International Journal of Electronics and Communication Engineering*, vol. 7, no. 5, pp. 10-18, 2020. Crossref, https://doi.org/10.14445/23488549/IJECE-V7I5P103

[23] J.-S. R. Jang, "ANFIS: Adaptive-Network-Based Fuzzy Inference System," *IEEE Transactions on Systems, Man, and Cybernetics*, vol. 23, no. 3, pp. 665–685, 1993. Crossref, https://doi.org/10.1109/21.256541

[24] J.-S. R. Jang and C. T. Sun, "Neuro-Fuzzy Modeling and Control," *Proceedings of the IEEE*, vol. 83, no. 3, pp. 378–406, 1995. Crossref, https://doi.org/10.1109/5.364486

[25] J.-S. Jang, C. T. Sun, and E. Mizutani, *"Neuro-Fuzzy and Soft Computing,"* Englewood Cliffs, NJ, USA: Prentice-Hall, 1997.

[26] Omorogiuwa Eseosa, Adesaanu Eunice Ejiroro "Challenges and Way Forward of Renewables in Developing Energy Economy: Today and Tomorrow," *International Journal of Recent Engineering Science*, vol. 7, no. 4, pp. 14-19, 2020. Crossref, https://doi.org/10.14445/23497157/IJRES-V7I4P103

[27] G. Dastagir and L. A. C. Lopes, "Voltage and Frequency Regulation of a Stand-Alone Self-Excited Induction Generator," *IEEE Canada Electrical Power Conference*, Montreal, QC, Canada, pp. 502–506, 2007. Crossref, https://doi.org/10.1109/EPC.2007.4520383

[28] Guohai Liu, Lingling Chen, Wenxiang Zhao, Yan Jiang, Li Qu, "Internal Model Control of Permanent Magnet Synchronous Motor Using Support Vector Machine Generalized Inverse," *IEEE Transactions on Industrial Informatics*, vol. 9, no. 2, pp. 890-898, 2013. Crossref, https://doi.org/10.1109/TII.2012.2222652

[29] L. Zhang, Z.Wang, X. Hu, F. Sun, and D. G. Dorrell, "Acomparative Study of Equivalent Circuit Models of Ultracapacitors for Electric Vehicles," *Journal of Power Sources*, vol. 274, pp. 899– 906, 2015. Crossref, https://doi.org/10.1016/j.jpowsour.2014.10.170

[30] S. Hala, N. Khalil Faris, and N. Khaled Faris, "Ultracapacitor: Modelling and Characterization for Electric Vehicle Application," *International Journal of Engineering Research*, vol. 5, no. 8, pp. 681– 686, 2016.